

EXPLORING THE OPTIMAL CHOICE FOR GENERATIVE PROCESSES IN DIFFUSION MODELS: ORDINARY VS STOCHASTIC DIFFERENTIAL EQUATIONS

YU CAO*, JINGRUN CHEN†, YIXIN LUO‡, AND XIANG ZHOU¶

ABSTRACT. The diffusion model has shown remarkable success in computer vision, but it remains unclear whether ODE-based probability flow or SDE-based diffusion models are superior and under what circumstances. Comparing the two is challenging due to dependencies on data distribution, score training, and other numerical factors. In this paper, we examine the problem mathematically by examining two limiting scenarios: the ODE case and the large diffusion case. We first introduce a pulse-shape error to perturb the score function and analyze error accumulation, with a generalization to *arbitrary error*. Our findings indicate that when the perturbation occurs at the end of the generative process, the ODE model outperforms the SDE model (with a large diffusion coefficient). However, when the perturbation occurs earlier, the SDE model outperforms the ODE model, and we demonstrate that the error of sample generation due to pulse-shape error can be exponentially suppressed as the diffusion term's magnitude increases to infinity. Numerical validation of this phenomenon is provided using toy models such as Gaussian, Gaussian mixture models, and Swiss roll. Finally, we experiment with MNIST and observe that varying the diffusion coefficient can improve sample quality even when the score function is not well trained.

1. INTRODUCTION

Diffusion models have achieved remarkable success in various artificial intelligence context generation tasks, particularly in computer vision [12]. This technique is rapidly evolving with industrial-level products like DALL·E 2. The diffusion model was first proposed and studied by Sohl-Dickstein et al. [21] in 2015. Later, Song and Ermon [24] proposed score matching with Langevin dynamics (SMLD) and Ho et al. [15] further explored the Denoising Diffusion Probabilistic Models (DDPM). Both formalisms can be interpreted as time-discretization of stochastic differential equations (SDEs) [25]. Since the publication of these seminal works, many techniques have been proposed to improve the efficiency and accuracy of diffusion models, such as DDIM [23], Analytic-DPM [4], gDDIM [31], and consistency model [26], among others.

The score-based diffusion model involves two steps [25, 16]. Firstly, one estimates the score function, which is the gradient of the logarithm of the probability density function, in the form of a neural network. This estimation step utilizes trajectories of an Ornstein-Uhlenbeck (OU) process starting with given data samples. This OU process of injecting noise into structured data is usually referred to

(*) INSTITUTE OF NATURAL SCIENCES & SCHOOL OF MATHEMATICAL SCIENCES, SHANGHAI JIAO TONG UNIVERSITY, SHANGHAI 200240, CHINA

(†,‡) UNIVERSITY OF SCIENCE AND TECHNOLOGY OF CHINA, HEFEI 230026, CHINA; SUZHOU INSTITUTE OF ADVANCED RESEARCH, UNIVERSITY OF SCIENCE AND TECHNOLOGY OF CHINA, SUZHOU 215123, CHINA

(¶) SCHOOL OF DATA SCIENCE AND DEPARTMENT OF MATHEMATICS, CITY UNIVERSITY OF HONG KONG, KOWLOON, HONG KONG SAR

E-mail addresses: yucao@sjtu.edu.cn, jingrunchen@ustc.edu.cn, seeing@mail.ustc.edu.cn, xizhou@cityu.edu.hk.

as the *inference process*. Secondly, new data samples are generated by simulating a time-reversed SDE, with a drift term that depends on the learned score function from the first step. This is known as the *generative process*.

In general, there are two diffusion coefficients g in the inference process and h in the generative process; See § 2. Regardless of the choice of diffusion coefficients (h and g), it is always possible to design an SDE in the generative process that matches the forward inference process in the weak sense, meaning that the probability density functions match for both processes. We highlight that this function h (unlike g) does not only appear in the diffusion term, but also enters the drift term in the generative SDE. The choice of g is equivalent to time re-scaling (see Appx. B.2), while the choice of h is an important topic in practice. Two common choices of h are Probability Flow $h = 0$ [9, 27], which refers to an ODE, and an SDE-based diffusion model with $h = g$ [15, 24, 25]. When the score training is accurate, the choice of this function does not affect the sample generation quality in the continuous time setting.

In practice, numerical error is inevitable during training the score function. Recent theoretical works [10, 7] have shown that the sample generation quality are affected by three aspects: (1) the truncation of simulation time to a finite T ; (2) the inexact score function; (3) the discretization error due to time step size. The first error is not significantly since the forward OU process converges to the equilibrium Gaussian measure exponentially fast in T . The third error can be improved by using more efficient numerical schemes [19], such as exponential integrator proposed in [30, 31]. The inexact training of score function has a few important but subtle consequences. Recent works [10, 7] analyzed the convergence rate of diffusion models provided the score training error is sufficient small. However once the score training is not accurate, the nice equivalence of the generated distribution free of the generative diffusion coefficient h no longer holds as in the idealized situation of exact score function. This raises a key question of our interest about how the choice of h can affect the sample quality in the face of the inexact score training error. Qualitatively, there are two distinctive cases: $h = 0$ or h is large. An important question to ask is: **in the presence of non-negligible score training errors, which choice of h will produce better sampling quality?** Is it the probability flow ($h = 0$) or the SDE? More quantitatively, what magnitude of the generative diffusion coefficient h is optimal?

Related works. The impact of h on the generative process seems not yet fully investigated in recent literature, as most experiments used the default choice of this parameter. However, some authors have reported related empirical observations. For example, Song et al. [25] empirically observed that the choice of $h = g$ produces better sample generation quality than the ODE case ($h = 0$) with real datasets. On the other hand, Denoising Diffusion Implicit Models (DDIM) in [23] includes both deterministic and stochastic samplers and points out that the probability flow ($h = 0$) can produce better samples with improved numerical schemes for generative process. [31] generalized the DDIM and tried to explain the advantages of a deterministic sampling scheme over the stochastic one for fast sampling. None of these empirical results delivered comprehensive investigations of the influence of the diffusion coefficient, and a consistent and affirmative answer to our question still awaits. Recently, there has been rapid progress in theoretical works on error analysis for diffusion models, as seen in [10, 7] and references therein. However, these analyses usually assume specific settings of h , such as $h = g$. Furthermore, efforts to analyze upper bounds based on these error estimations have failed to provide adequate information about choosing the optimal h . See our discussion in Appx. B.4. Albergo et al. [1, Sec. 2.4] briefly discussed the optimal choice between the probability flow and diffusion models but in a different framework than the score-based diffusion models herein.

Our approach. To investigate the effect of the diffusion coefficient h on sampling quality, we adopt the continuous-time framework, which precludes time discretization errors. We measure sample quality by the KL divergence between the data distribution p_0 and the distribution of the generative SDE at the terminal time T . Given the assumption that the score function carries numerical errors, we consider h as a controller and aim to minimize the KL divergence with respect to h . While the optimization problem is straightforward, it is challenging to draw valuable theoretical insights in a general setting of approximate score functions. Therefore, we choose the asymptotic approach, assuming that the error from the training score is reasonably small with a magnitude of ϵ . Under this assumption, the leading-order term of the KL divergence takes the form

$$\text{error of sample generation in KL divergence} = L(h) \epsilon^2 + \mathcal{O}(\epsilon^3).$$

This ϵ^2 order is known in [7, 10], but the dependence of this Gateaux differential $L(h)$ on h and other factors has yet to be understood at all. Our contribution is to analyze how $L(h)$ behaves as h varies; in particular, by considering the constant h in two limiting situations: $h = 0$ and $h \gg 1$.

Main Contributions. We summarize main contributions below:

- We prove that when the error in score function approximation is a time-localized function only at the beginning of the inference step (i.e., at the end of the generative process), the ODE case ($h = 0$) outperforms the SDE case ($h \rightarrow \infty$); see Prop. 3.5. If this (time-localized) error occurs in the middle, then the SDE case has the *exponentially smaller error* than the ODE case ($h = 0$), as $h \rightarrow \infty$; see Prop. 3.4.
- For a general type of score training error, we prove that as $h \rightarrow \infty$, the leading-order term $L(h)$ above converges to a positive *constant* exponentially fast, and this constant only depends on the data distribution p_0 and the score training error at the *end* of the generative process; see Prop. 3.6. The conclusion about difference in various h depends on the how the score training error is distributed over the time horizon $[0, T]$.

Numerically, we validate the above phenomenon for 1D Gaussian, 2D Gaussian mixture, and Swiss roll distribution. Our results may suggest different strategy of picking up h when various weight methods are used in training the score functions.

Notation convention. The time duration $T > 0$ is a fixed parameter throughout this paper. For any time-dependent function $(t, x) \mapsto f_t(x)$, where $x \in \mathbb{R}^d$ and $t \in [0, T]$, we denote $f_t^\leftarrow(x) \equiv f_{T-t}(x)$. In many cases, we may directly use the “arrowed” variables $f_t^\leftarrow(x)$ to highlight the direction of time is from reference noise to the data distribution (i.e., the generative time direction) even without referring to f first. When we write $f \lesssim g$, it means $f \leq cg$ where $c \rightarrow 1$ in a certain limit, namely, $\limsup f/g \leq 1$; $f \sim g$ means $\lim(f/g) = 1$. The asymptotic parameter will be explained below explicitly. When two matrices $A \preceq B$, it means $B - A$ is positive semidefinite. \mathbf{I}_d means d -dimensional identity matrix; \mathbb{I}_A means an indicator function of the set A ; Id means the identity operator. For a random variable, e.g., X , $\text{law}(X)$ means the distribution of X . Some important quantities defined in later sections are summarized in Appx. A.

2. BACKGROUND

Score-based generative models. Suppose we have a collection of data from an unknown distribution with density p_0 , we can inject noise into data via the following SDEs:

$$(1) \quad dX_t = f_t(X_t) dt + g_t dW_t, \quad \text{law}(X_0) = p_0,$$

where the drift coefficient $f_{(\cdot)}(\cdot) : \mathbb{R}^d \times \mathbb{R} \rightarrow \mathbb{R}^d$ is a time-dependent vector field, and the diffusion coefficient $g_{(\cdot)} : \mathbb{R} \rightarrow \mathbb{R}$ is a scalar-valued function (for simplicity). A widely used example is variance-preserving SDE (VP-SDE) with $f_t(x) = -1/2 g_t^2 x$ and $g > 0$ is typically chosen as a non-decreasing function in literature [25]. Without loss of generality, we can assume $g_t = 1$ since for any non-zero g , its effect is simply to re-scale the time; see Appx. B.2.

Denote the probability density of X_t as p_t . The score function is defined as $\nabla \log p_t(x)$. One of main innovations in the score-based diffusion models is to find a “backward” SDE Y_t such that Y_t drives the state with distribution p_T back to p_0 . We adopt the arrow of time in this backward direction now and write Y_t as

$$(2) \quad dY_t = A_t^\leftarrow(Y_t) dt + h_t^\leftarrow dW_t, \quad \text{law}(Y_0) = p_T,$$

where h_t^\leftarrow is an arbitrary real-valued function of time. The distribution of Y_t is denoted as q_t . Provided that the score function is available, we can select A_t^\leftarrow such that q_t is the same as p_{T-t} , in particular, $q_T = p_0$. It is not hard to derive that we can ensure $q_t \equiv p_{T-t}$ if we choose

$$(3) \quad A_t^\leftarrow(x) = -f_t^\leftarrow(x) + \frac{(g_t^\leftarrow)^2 + (h_t^\leftarrow)^2}{2} \nabla \log p_t^\leftarrow(x).$$

The proof is provided in Appx. B.1. This result generalizes [25]: when $h^\leftarrow = g^\leftarrow$, it refers to the backward SDE used in [25]; when $h^\leftarrow = 0$, it refers to the probability flow therein. More general interpolation of diffusion and flow can be found in, e.g., [1].

Source of errors. In practice, the score function $(t, x) \mapsto \nabla \log p_t^\leftarrow(x)$ needs to be trained from data. Hence, there is intrinsic error often times due to an inexact score function, which might come from many scenarios, e.g., there is only a finite amount of samples of p_0 available or only a small neural network architecture is achievable. However, it is reasonable to assume that this non-negligible error is insignificant. Hence, we decompose the numerically trained score function $\mathfrak{S}_t^\leftarrow$ into

$$(4) \quad \mathfrak{S}_t^\leftarrow(x) = \nabla \log p_t^\leftarrow(x) + \epsilon \mathcal{E}_t^\leftarrow(x),$$

where ϵ is small, $\mathcal{E}_t^\leftarrow(x)$ is assumed to at order one and the total error is $\epsilon \mathcal{E}_t^\leftarrow$.

In addition, we understand the generative process used in practice has to use $\text{law}(Y_0) = \mathcal{N}(0, I_d)$ instead since p_T is not intractable in (2). But by choosing T large enough so that $p_T \approx \mathcal{N}(0, I_d)$, we can neglect this error due to finite T in our analysis. Besides, we also need some numerical schemes to simulate this generative SDE, which also leads into discretization errors. **In summary**, there are three sources of errors (1) $p_T \neq \mathcal{N}(0, I_d)$: this is the source of errors in the initial distribution of the generative process; (2) $\mathcal{E}^\leftarrow \neq 0$: error from imperfect score function from training; (3) numerical discretization of the generative process. The third error can be systematically eliminated by choosing a high-order scheme [19] or an extremely small time step. It has been observed that by choosing a more accurate numerical scheme, e.g., exponential integrator, one can reduce the computational costs [30, 31]. As for the first error, if one chooses the OU process for (1), p_T converges to $\mathcal{N}(0, I_d)$ exponentially fast and thus $T = \mathcal{O}(\ln(\delta))$ where δ is the error between p_0 and the distribution of generated samples. Therefore, the choice of T is, in practice, not hard to manage. More details about how these three error sources contribute to the sample generation quality can be found in, e.g., [7, 10] or the discussion in Appx. B.3.

3. ASYMPTOTIC ANALYSIS OF TERMINAL ERRORS

We use the KL divergence between the data distribution p_0 and the distribution of generated samples to quantify the performance of generative model, which depends on the error of score function

$\epsilon \mathcal{E}^{\leftarrow}$, the diffusion coefficient h^{\leftarrow} , and data distribution p_0 . To extract the main feature, we first let $\epsilon \rightarrow 0$ and estimate

$$\text{sample generation error in KL divergence} = L(h^{\leftarrow}, \mathcal{E}^{\leftarrow}, p_0) \epsilon^2 + \mathcal{O}(\epsilon^3).$$

Whenever p_0 and \mathcal{E}^{\leftarrow} are obvious from the context, we simply write $L(h^{\leftarrow}) \equiv L(h^{\leftarrow}, \mathcal{E}^{\leftarrow}, p_0)$. Next, we formulate the main problem setup and assumptions in § 3.1. The expression of L is shown in Prop. 3.2. Then we let $h_t^{\leftarrow} \equiv h$ be independent of time, and study how the leading order function L depends on h in various settings of error function $\mathcal{E}_t^{\leftarrow}$. Firstly, we consider $\mathcal{E}_t^{\leftarrow} = \delta_{t-s} E(x)$ as a time-localized function and two limiting scenarios: $h^{\leftarrow} = h$ where $h = 0$ (ODE case) and $h \rightarrow \infty$ (SDE case with large diffusion). When $\mathcal{E}_t^{\leftarrow} = \delta_{t-s} E(x)$ is a time-localized function at the end of the generative process (i.e., s is close to T), the ODE case will outperform the SDE case (see Prop. 3.5); otherwise, the SDE case has an exponentially smaller error than the ODE case as $h \rightarrow \infty$ (see Prop. 3.4). Secondly, by combining Prop. 3.4 and Prop. 3.5, the tail behavior of $h \mapsto L(h)$ for a general \mathcal{E}^{\leftarrow} is described in Prop. 3.6.

3.1. Set-up and assumptions. We fix the time T and consider the following SDE for the generative process in $t \in [0, T]$,

$$(5) \quad d\tilde{Y}_t = \left(-f_t^{\leftarrow}(\tilde{Y}_t) + \frac{(g_t^{\leftarrow})^2 + (h_t^{\leftarrow})^2}{2} \mathfrak{S}_t^{\leftarrow}(\tilde{Y}_t) \right) dt + h_t^{\leftarrow} dW_t, \quad \text{law}(\tilde{Y}_0) = p_T,$$

which can be regarded as a perturbed equation (2) of Y_t . Denote the distribution of \tilde{Y}_t as \tilde{q}_t . Note that \tilde{q}_T depends on both $\mathfrak{S}_t^{\leftarrow} = \epsilon \mathcal{E}_t^{\leftarrow}$ and h^{\leftarrow} ; however, when $\epsilon = 0$, by (3), $\tilde{q}_T \equiv q_T \equiv p_0$ for any h^{\leftarrow} . We quantify the sample generation quality via

$$\text{KL}(p_0 || \tilde{q}_T) = \int p_0 \log \frac{p_0}{\tilde{q}_T}.$$

Due to the presence of $\epsilon \mathcal{E}^{\leftarrow}$ with non-zero ϵ , in general $\text{KL}(p_0 || \tilde{q}_T) > 0$.

Assumption 3.1. *Throughout this section, we assume that:*

- (1) *For the forward process, we assume $f_t(x) = -\frac{1}{2}x$, $g_t = 1$ without loss of generality.*
- (2) *The data distribution has the density p_0 .*
- (3) *There exists a number $c_U \in \mathbb{R}$ such that $U_0(x) - |x|^2/2 \geq c_U$, for any $x \in \mathbb{R}^d$, where $U_0 = -\log p_0$.*

Recall that a generic g_t is equivalent to time re-scaling (Appx. B.2), So this choice of $g_t = 1$ refers to the generic choice in VP-SDE [25]. The second assumption is also very mild; in practice, if p_0 is a delta distribution, a common practice is that one tries to learn the mollified version $p_\sigma(x) := \int_{\mathbb{R}^d} \frac{1}{(2\pi\sigma^2)^{d/2}} \exp(-|x-y|^2/2\sigma^2) p_0(y) dy$ instead, as in the GAN [22] and early-stop techniques [7, 10]. The third assumption is not restrict, for example, $U_0(x) = |x|^2$ and $c_U = 0$. Since most realistic datasets are effectively in low-dimensional subspaces [17, 5], this assumption is reasonable.

3.2. Asymptotic expansion of the KL divergence with respect to ϵ . We first need to introduce a time-dependent operator

$$(6) \quad \mathcal{L}_t^{(h^{\leftarrow})}(\mu)(x) := -\nabla \cdot \left(\left(\frac{1}{2}x + \frac{1 + h_t^{\leftarrow-2}}{2} \nabla \log p_t^{\leftarrow}(x) \right) \mu(x) \right) + \frac{h_t^{\leftarrow-2}}{2} \Delta \mu(x),$$

which is the generator in the Fokker-Planck equation of q_t for (2). Define an operator $\Phi_{s,t}^{(h^{\leftarrow})}$ as follows: given any function μ , define $\Phi_{s,t}^{(h^{\leftarrow})}(\mu)$ to be the solution at time t of the following Fokker-Planck equation with $r \in [s, t]$: $\partial_r \theta_r = \mathcal{L}_r^{(h^{\leftarrow})}(\theta_r)$, and with initial condition $\theta_s = \mu$. We define $\Phi_{s,t}^{(h^{\leftarrow})}(\mu) := \theta_t$. Properties of this operator are collected in Appx. C.1.

We use the notation \tilde{q}^ϵ to refer to \tilde{q} since we need calculate the its derivative for the small parameter ϵ . The dependence of \tilde{q} on h^\leftarrow is suppressed for short notations. We have the following asymptotic result with the proof given in Appx. C.3.

Proposition 3.2. *Define $v_T := \partial_\epsilon \tilde{q}_T^\epsilon|_{\epsilon=0}$ as the first-order perturbation of \tilde{q}_T^ϵ . We have*

$$(7) \quad KL(p_0||\tilde{q}_T^\epsilon) = L(h^\leftarrow)\epsilon^2 + \mathcal{O}(\epsilon^3),$$

where

$$(8) \quad L(h^\leftarrow) = \frac{1}{2} \int_{\mathbb{R}^d} \frac{v_T^2(x)}{p_0(x)} dx, \quad v_T = -\frac{1}{2} \int_0^T (1 + h_t^{\leftarrow 2}) \Phi_{t,T}^{(h^\leftarrow)} (\nabla \cdot (p_t^\leftarrow \mathcal{E}_t^\leftarrow)) dt.$$

3.3. Multi-scale dynamics in the Fokker-Planck operator $\mathcal{L}_t^{(h^\leftarrow)}$ when $h^\leftarrow \gg 1$. Let the potential $U_t := -\log p_t$, and by conventions $U_t^\leftarrow \equiv U_{T-t}$. When $h^\leftarrow > 0$, we can rewrite

$$(9) \quad \mathcal{L}_t^{(h^\leftarrow)}(\mu) = h_t^{\leftarrow 2}/2 \left(\Delta \mu + \nabla \cdot (\nabla V_t^\leftarrow \mu) \right), \quad V_t^\leftarrow(x) := (1 + 1/h_t^{\leftarrow 2}) U_t^\leftarrow(x) - \frac{|x|^2}{2h_t^{\leftarrow 2}}.$$

We now introduce a probability distribution induced by the potential V_t^\leftarrow :

$$(10) \quad \rho_t^\leftarrow \propto \exp(-V_t^\leftarrow).$$

By convection, we also have $V_t = V_{T-t}^\leftarrow$ and $\rho_t = \rho_{T-t}^\leftarrow$. Note that V_t^\leftarrow depends on h^\leftarrow and when $h^\leftarrow \rightarrow \infty$, we have $V_t^{\leftarrow, \infty} = U_t^\leftarrow$.

The role of h^\leftarrow in $\mathcal{L}_t^{(h^\leftarrow)}$ now can be viewed as time re-scaling and the effect of $\mathcal{L}_t^{(h^\leftarrow)}$ at a local time t can be viewed as evolving the Fokker-Planck equation associated with the overdamped Langevin dynamics in the time-dependent potential V_t^\leftarrow for $\mathcal{O}(h_t^{\leftarrow 2}/2)$ amount of time. When $h^\leftarrow \rightarrow \infty$, $\mathcal{L}_t^{(h^\leftarrow)}$ can be roughly viewed as constructing an “almost quasi-static” thermodynamics [6] bridging the initial p_T and the (quasi-)equilibrium $p_0 = e^{-U_T^\leftarrow}$; see Appx. C.2 for more details. This key observation will guide our analysis of the solution operator $\Phi_{t,T}^{(h^\leftarrow)}$ appearing in Prop. 3.2.

3.4. Score function is perturbed by a pulse. From (8), we know that v_T combines the averaged effect of $\Phi_{t,T}^{(h^\leftarrow)}(\nabla \cdot (p_t^\leftarrow \mathcal{E}_t^\leftarrow))$ for various t . As a first result, we consider $\mathcal{E}_t^\leftarrow(x) = E(x)\delta_{t-s}$ for a fixed time instance $s \in [0, T]$, where δ_{t-s} is the Dirac function. In this case, v_T no longer involves time integration and we have

$$(11) \quad v_T = -\frac{(1 + h_s^{\leftarrow 2})}{2} \Phi_{s,T}^{(h^\leftarrow)}(\nabla \cdot (p_s^\leftarrow E)), \quad L(h^\leftarrow) = \frac{(1 + h_s^{\leftarrow 2})^2}{8} \int_{\mathbb{R}^d} \frac{(\Phi_{s,T}^{(h^\leftarrow)}(\nabla \cdot (p_s^\leftarrow E)))^2}{p_0}.$$

To proceed, we need to make additional assumptions:

Assumption 3.3.

(1) For any $t \in [0, T]$, $U_t = -\log p_t$ is assumed to be strongly convex and the Hessian of U_t is bounded by two positive numbers m_t and M_t as below

$$(12) \quad m_t \mathbf{I}_d \preceq \nabla^2 U_t(x) \preceq M_t \mathbf{I}_d, \quad \forall x \in \mathbb{R}^d.$$

Moreover, assume that

$$(13) \quad m_t \geq 1, \quad t \in [0, T].$$

(2) For all $t \in [0, T]$, we choose $h_t^\leftarrow = h$ as constant.

Introduce

$$(14) \quad \kappa_t^\leftarrow := (1 + \mathbf{h}^{-2})m_t^\leftarrow - \mathbf{h}^{-2} = (1 + \mathbf{h}^{-2})m_{T-t} - \mathbf{h}^{-2},$$

which characterizes the Hessian lower bound of V_t^\leftarrow (9). Note $\kappa_t^\leftarrow \approx m_t^\leftarrow$ when $\mathbf{h} \gg 1$. We would like to explain the reason behind the above assumptions, in particular, their practical relevance. *Part (i) Strong convexity:* this is a common assumption for Langevin sampling analysis [11, 13]. As the role of $\mathcal{L}_t^{(h^\leftarrow)}$ is essentially simulating a Langevin dynamics with time-dependent potential, it is reasonable to use this assumption as a starting point. Moreover, the algorithmic improvement in gDDIM [10] is highly inspired by a form with assuming the data distribution as a Gaussian; Fréchet inception distance (FID) [14], a widely used metric to evaluate the quality of generative model, essentially treats the data (in the feature space) as Gaussians. Therefore, we believe that this assumption can still capture some main features of realistic datasets. *Part (ii) $m_t \geq 1$ for any $t \in [0, T]$:* The second assumption $m_t \geq 1$ means that p_t is more localized (smaller variance) than the standard Gaussian (unit variance), which is compatible with Assumption 3.1 (3). This assumption is consistent with the so called manifold hypothesis used [5] since real data is usually on a low dimensional manifold [17]. This assumption can also ensure that V_t is strongly convex with positive Hessian lower bounds, i.e., $\kappa_t^\leftarrow > 0$, for any $t \in [0, T]$ and $\mathbf{h} \in (0, \infty)$.

Proposition 3.4. *Under Assumptions 3.1 and 3.3, suppose that $\mathcal{E}_t^\leftarrow(x) = E(x)\delta_{t-s}$ for some fixed $s \in [0, T]$. If $\mathbf{h} \geq \mathbf{h}_{lb} := \max \left\{ \frac{1}{2}, \mathbf{h}_0(1/2), \sqrt{\max\{0, -\frac{c_U}{\ln(2)}, \sup_{t \in [s, T]} C_t^{\leftarrow, (2)}\}} \right\}$, we have the upper bound of $L(\mathbf{h})$ in (11):*

$$(15) \quad L(\mathbf{h}) \leq C_{\mathbf{h}}(1 + \mathbf{h}^2)^2 \exp \left(- \int_s^T (\mathbf{h}^2 - C_r^{\leftarrow, (2)})\kappa_r^\leftarrow - C_r^{\leftarrow, (1)} dr \right),$$

where $C_{\mathbf{h}} = \frac{1}{2} \int (\nabla \cdot (p_s^\leftarrow E))^2 / \rho_s^\leftarrow$, $C_t^{\leftarrow, (2)} = \frac{20+30M_t^{\leftarrow-2}}{m_t^{\leftarrow-2}}$; see Appx. E for details about $C_t^{\leftarrow, (1)}$ and $\mathbf{h}_0(1/2)$; $c_U \in \mathbb{R}$ is from Assumption 3.1. Moreover, $\lim_{\mathbf{h} \rightarrow \infty} C_{\mathbf{h}}$, $\lim_{\mathbf{h} \rightarrow \infty} C_t^{\leftarrow, (1)}$ exist.

See Appx. E for proofs. The *main intuition* is that: if the error function \mathcal{E}_t^\leftarrow is a pulse at time $t = s$, then for a large \mathbf{h} , $L(\mathbf{h})$ will decay to zero exponentially fast. For 1D Gaussian case, we can clearly observe such an exponential decay in Fig. 1a, where we pick $\mathcal{E}_t^\leftarrow = \mathbb{I}_{t \leq 0.95T} \nabla \log p_t^\leftarrow$. The intuition behind this exponential suppressed prefactor is that for large h , $\Phi_{s,T}^{(h^\leftarrow)}$ can be viewed as an almost quasi-static thermodynamics dragging any positive measure towards $\rho_T^\leftarrow \approx p_0$, as mentioned above in § 3.3. As $\nu = \nabla \cdot (p_s^\leftarrow E)$ has measure zero, we can split it into positive and negative parts: $\nu = \nu^+ - \nu^-$ (assume $\int \nu^\pm = 1$ WLOG). Each term $\Phi_{s,T}^{(h^\leftarrow)}(\nu^+) \approx \rho_T^\leftarrow \approx \Phi_{s,T}^{(h^\leftarrow)}(\nu^-)$, which explains that $\Phi_{s,T}^{(h^\leftarrow)}(\nu) \approx 0$ for large \mathbf{h} .

3.5. Score function is only perturbed near the end of the generative process.

Proposition 3.5. *Under Assumptions 3.1 and 3.3, suppose that $\mathcal{E}_t^\leftarrow(x) = \mathbb{I}_{t \in [T-a, T]} E(x)$ where $a \ll 1$. Then when $a \ll 1$ and $\mathbf{h} \gg 1$, asymptotically ,*

$$L(0) \sim \frac{a^2}{8} \int_{\mathbb{R}^d} \frac{(\nabla \cdot (p_0 E))^2}{p_0}, \quad L(\mathbf{h}) \lesssim \frac{(1 - e^{-a \frac{\mathbf{h}^2}{2} \kappa_0})^2}{2\kappa_0^2} \int_{\mathbb{R}^d} \frac{(\nabla \cdot (p_0 E))^2}{p_0},$$

with $\kappa_0 = (1 + \frac{1}{\mathbf{h}^2})m_0 - \frac{1}{\mathbf{h}^2}$ as in (14). The upper bound of $L(\mathbf{h})$ is tight asymptotically.

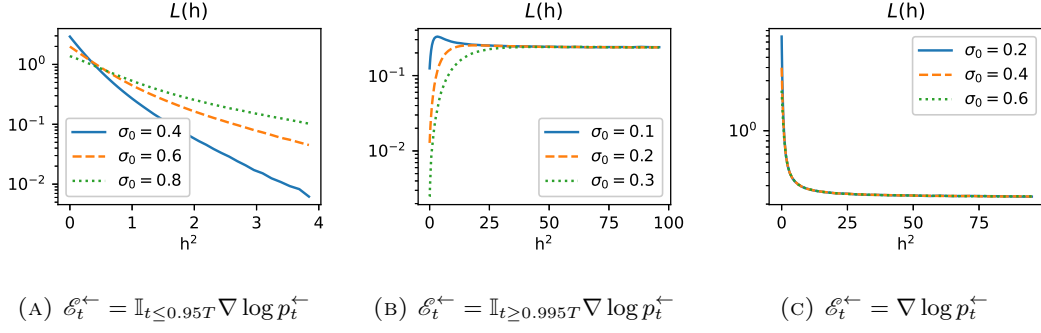


FIGURE 1. 1D Gaussian $p_0 = \mathcal{N}(0, \sigma_0^2)$ (with different σ_0 smaller than one) and $T = 2$. Panel (a) validates the exponential decay of $L(h)$ when the score function has no error near $t \approx T$, similar to Prop. 3.4. Panel (b) validates Prop. 3.5 that the ODE model ($h = 0$) outperforms the SDE model when there is a large score error at $t \approx T$. Panel (c) validates Prop. 3.6 that $\lim_{h \rightarrow \infty} L(h)$ exists.

We remark that we made *no assumption on how ah^2 scales*. When $h \gg 1$, $L(h)/L(0) \lesssim 4(1 - e^{-a\frac{h^2}{2}\kappa_0})^2/a^2\kappa_0^2$. **Case (I):** If $ah^2 \gg 1$, then $L(h)/L(0) \lesssim 4/a^2\kappa_0^2$, which is large as $a \ll 1$. **Case (II):** If $ah^2 \ll 1$, then $L(h)/L(0) \lesssim h^4$, which is still large. In either case, asymptotically, $L(h)/L(0)$ is expected to be extremely large for a general E and the ODE model is preferred in this case. The intuition is that there is almost no time for the operator $\mathcal{L}_t^{(h^{\leftarrow})}$ to suppress the error E , so the prefactor $1 + (h_t^{\leftarrow})^2$ in v_T (8) dominates.

The proof is in Appx. F. In Fig. 1b, we consider the 1D Gaussian and only perturb the score function at the end of the generative process ($\mathcal{E}_t^{\leftarrow} = \mathbb{I}_{t \geq 0.995T} \nabla \log p_t^{\leftarrow}$). We can clearly observe that the SDE-based models has larger error compared with the ODE-based model.

3.6. General error in score function. We can generalize Prop. 3.4 and 3.5 to a general error function \mathcal{E}^{\leftarrow} , and observe that $L(h)$ will converge to a constant exponentially fast.

Proposition 3.6. *Under Assumptions 3.1 and 3.3, we consider a general error function $\mathcal{E}_t^{\leftarrow}(x)$. Let $\gamma = \inf_{h \geq h_{lb}} \inf_{t \in [0, T]} \kappa_t^{\leftarrow}$. For any $\alpha \in (0, 1)$ and $\beta \in (0, 2)$, when $h \gg 1$,*

$$\begin{aligned} L(h) &\lesssim (1 + \alpha^2)\mathcal{T} + (1 + \alpha^{-2})C\gamma^{-1}(1 + h^2)\exp(-h^{2-\beta}\gamma), \\ L(h) &\gtrsim (1 - \alpha^2)\mathcal{T} - (\alpha^{-2} - 1)C\gamma^{-1}(1 + h^2)\exp(-h^{2-\beta}\gamma), \end{aligned}$$

where C is given in Appx. G and the positive constant \mathcal{T} (only depending on p_0 and $\mathcal{E}_T^{\leftarrow}$) is upper bounded by

$$\mathcal{T} \lesssim \frac{1}{2m_0^2} \int_{\mathbb{R}^d} \frac{(\nabla \cdot (p_0 \mathcal{E}_T^{\leftarrow}))^2}{p_0}.$$

We can notice that in the limit of $h \rightarrow \infty$, $(1 - \alpha^2)\mathcal{T} \lesssim L(h) \lesssim (1 + \alpha^2)\mathcal{T}$, where $\alpha \in (0, 1)$ is arbitrary. Hence, the tail behavior is that $L(h)$ converges to \mathcal{T} exponentially fast as $h \rightarrow \infty$. If we assume that $\mathcal{E}_T^{\leftarrow} = \nabla \log p_0$, $p_0 = \mathcal{N}(0, \sigma_0^2)$ in one dimension, then the above upper bound is simply $\mathcal{T} \lesssim 1$, which is independent of p_0 . For 1D Gaussian in Fig. 1c, we can indeed observe that $\lim_{h \rightarrow \infty} L(h)$ exists, and is bounded above by 1; see Appx. H for more examples.

4. NUMERICAL EXPERIMENTS

We present experiments on 2D Gaussian mixture model, Swiss roll, and MNIST to support our theoretical results. The details of datasets, network architectures, hyper-parameters for training and evaluation metrics are presented in Appx. I. More numerical results are presented in Appx. J. Our source codes will be available at <https://anonymous.4open.science/r/OptimalDiffusion-FEOC/>.

2D 4-mode Gaussian mixture. In Fig. 2, a clear trend is that a higher h produces generated distributions that better match the marginal densities, and it is numerically verified by the purple line of Fig. 3a. In Fig. 3, with multiple settings of \mathcal{E}_t^\leftarrow and ϵ , we see a consistent result that as h increases, the KL divergence of true data and generated data converges exponentially fast, thus validating Prop. 3.6. It worths noticing that in all three settings of \mathcal{E}_t^\leftarrow , by simply applying larger h in (3), we can obtain better generative models without any extra training costs. We present the results of the 1D Gaussian mixture in Appx. J.

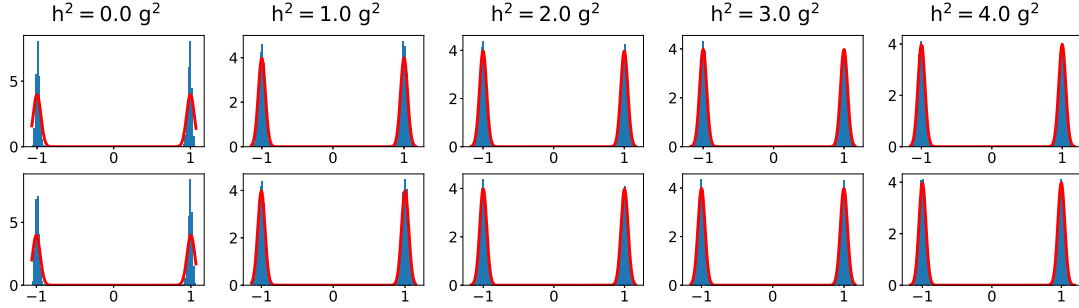


FIGURE 2. Visualization of marginal densities of 2D 4-mode Gaussian mixture, where $\mathcal{E}_t^\leftarrow = \nabla \log p_t^\leftarrow$ and $\epsilon = 0.2$. The top row shows the marginal distribution of the first coordinate and the bottom row shows the marginal distribution of the second coordinate. The red lines characterize the exact marginal distributions of p_0 and the histograms (blue) visualize the empirical densities of generated samples.

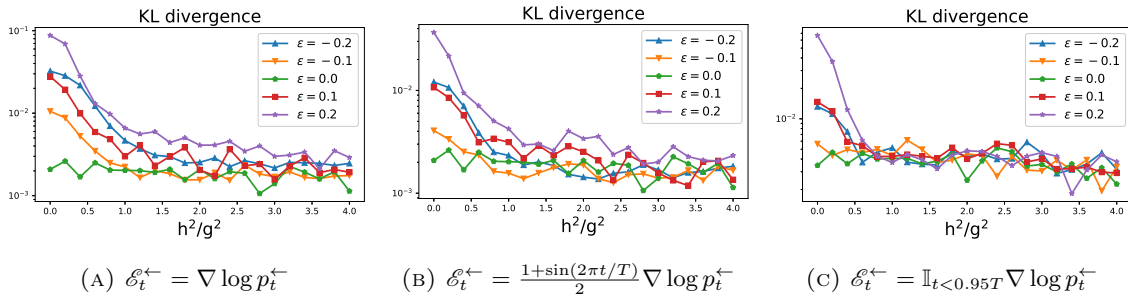
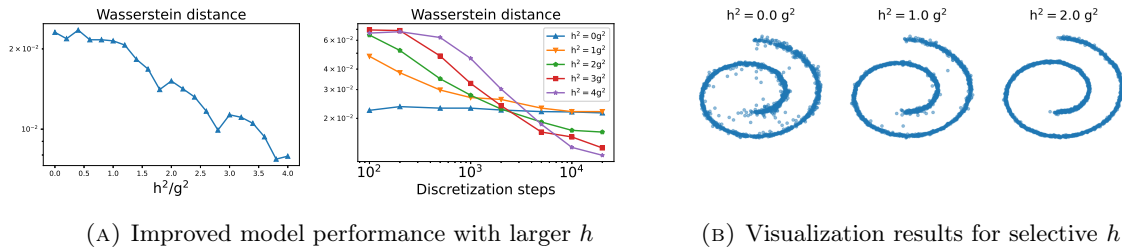


FIGURE 3. Numerical results of 2D 4-mode Gaussian mixture. The above panels show that the KL divergences between the true distribution and the generated samples overall decay as h increases for various types of error perturbation of score functions.

Swiss roll. We consider a more complex data distribution without exact score function available: Swiss roll. We train the score function with the denoising score-matching objective [28] (Appx. I). The first plot in Fig. 4a shows the difference between true data and generated data measured by the Wasserstein distance, which converges to zero exponentially fast, verifying Prop. 3.6. In the second plot of Fig. 4a, we tested various h and the number of time steps for generative process. The ODE model ($h = 0$) does not improve the quality as the number of time discretization steps increases, but we see that near the continuous time limit, all SDE cases ($h > 0$) are better than the ODE model. This suggests that our conclusions in this paper may limit to continuous time setting. The exploration of time discretization errors will be future works.

The generated data results in Fig. 4b clearly demonstrate that with an increasing h , the sample quality are improved. More results of Swiss roll are presented in Appx. J.



(A) Improved model performance with larger h (B) Visualization results for selective h

FIGURE 4. Numerical results of Swiss roll. Panel (a) shows the decay of Wasserstein distance between the true distribution and the generated samples with increasing h and 20,000 time discretization steps, and the decay of Wasserstein distance with the increasing number of time discretization steps and different h . Panel (b) shows generated samples with different h .

MNIST. Our study suggests that models with large diffusion coefficients are more negatively affected by score error at the terminal time $t \approx T$. In contrast, the ODE case is more negatively affected by the score training error corresponding to the early stage of the generative process. We test these practical hints from our theories on the MNIST dataset. To control the score error during the training, we deliberately use a small network architecture and adopt different weight schemes in the loss function for training (see Appx. I): (1) data-driven: more weight in the data side; (2) default: the one in [25]; (3) noise-driven: more weight in the noise side. The time with higher weights naturally suggests a lower training error there. Firstly, we verified that increasing the weight in the noise side appears to improve the sample generation quality of ODE-based models; see Fig. 5. Secondly, we observe that larger diffusion coefficients can improve the sample generation quality by testing various diffusion magnitude h^2/g^2 and time-discretization steps; see Appx. J, where the results there can be explained by Prop. 3.4: score-training error from the initial stage of the generative process can be “washed away” with larger h , so that the state in the generative process will move into the importance region of true dataset, which leads into a reasonable image with larger probability (as long as the numerical integrator is reasonably accurate).

5. SUMMARY AND OUTLOOK

In this work, we study the effect of the diffusion coefficient on the quality of overall sample generation in the generative process. Theoretically, we provide understandings of scenarios in which ODE-based

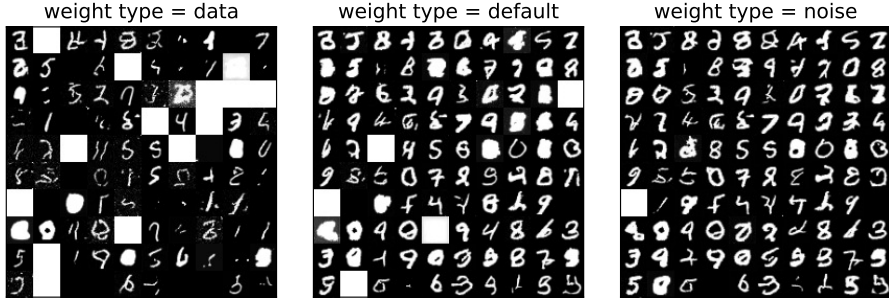


FIGURE 5. We show generated samples trained for MNIST using three different weight functions in the loss function: we use $h^2/g^2 = 0$ (ODE), time step is 1000, the trial number is 1 (the index for independent random initialization).

models and SDE-based models are superior than each other; see Propositions 3.4 and 3.5. Numerically, these results are validated via 1D Gaussian, 2D Gaussian mixture models, Swiss roll, as well as the benchmark dataset MNIST. There are many interesting directions for continuing works: (1) Can we design a practical criterion that directly learn the optimal magnitude of h by looking at the score-training error distribution? (2) How can we find a stable and accurate numerical scheme to deal with fast diffusion case? (3) How can we generalize theoretical results by removing the convexity assumption, and including the low-dimensional feature of datasets into the theory [8]?

ACKNOWLEDGMENT

The work of J. Chen and Y. Luo is supported by the National Key R&D Program of China (2022YFA1005200, 2022YFA1005203), by the NSFC Major Research Plan - Interpretable and General-purpose Next-generation Artificial Intelligence (92270001, 92270205), by the Anhui Center for Applied Mathematics, and by the Major Project of Science & Technology of Anhui Province (202203a05020050). The work of X. Zhou is partially supported by Hong Kong RGC GRF 11307319, 11308121, 11318522, and the NSFC/RGC Joint Research Scheme [RGC Project No. N-CityU102/20 and NSFC Project No. 12061160462].

REFERENCES

- [1] Michael S. Albergo, Nicholas M. Boffi, and Eric Vanden-Eijnden. Stochastic Interpolants: A Unifying Framework for Flows and Diffusions, 2023. arXiv:2303.08797 [cond-mat].
- [2] D. Bakry and M. Émery. Diffusions hypercontractives. In *Lecture Notes in Mathematics*, pages 177–206. Springer Berlin Heidelberg, 1985. doi: 10.1007/bfb0075847. URL <https://doi.org/10.1007/bfb0075847>.
- [3] Dominique Bakry, Ivan Gentil, and Michel Ledoux. *Analysis and Geometry of Markov Diffusion Operators*. Springer International Publishing, 2014. doi: 10.1007/978-3-319-00227-9. URL <https://doi.org/10.1007/978-3-319-00227-9>.
- [4] Fan Bao, Chongxuan Li, Jun Zhu, and Bo Zhang. Analytic-DPM: an analytic estimate of the optimal reverse variance in diffusion probabilistic models. In *International Conference on Learning Representations*, 2022. URL <https://openreview.net/forum?id=0xiJLKH-ufZ>.
- [5] Valentin De Bortoli. Convergence of denoising diffusion models under the manifold hypothesis. arxiv 2208.05314. 2022.

- [6] Herbert B Callen. *Thermodynamics and an Introduction to Thermostatistics*. John Wiley & Sons, Nashville, TN, 2 edition, August 1985.
- [7] Hongrui Chen, Holden Lee, and Jianfeng Lu. Improved Analysis of Score-based Generative Modeling: User-Friendly Bounds under Minimal Smoothness Assumptions. 2022. arXiv: 2211.01916.
- [8] Minshuo Chen, Kaixuan Huang, Tuo Zhao, and Mengdi Wang. Score Approximation, Estimation and Distribution Recovery of Diffusion Models on Low-Dimensional Data, February 2023.
- [9] Ricky T. Q. Chen, Yulia Rubanova, Jesse Bettencourt, and David K Duvenaud. Neural Ordinary Differential Equations. In *Advances in Neural Information Processing Systems*, volume 31. Curran Associates, Inc., 2018. URL <https://papers.nips.cc/paper/2018/hash/69386f6bb1dfed68692a24c8686939b9-Abstract.html>.
- [10] Sitan Chen, Sinho Chewi, Jerry Li, Yuanzhi Li, Adil Salim, and Anru Zhang. Sampling is as easy as learning the score: theory for diffusion models with minimal data assumptions. In *The Eleventh International Conference on Learning Representations*, 2023. URL <https://openreview.net/forum?id=zyLVMgsZOU>.
- [11] Xiang Cheng and Peter Bartlett. Convergence of Langevin MCMC in KL-divergence. In *Algorithmic Learning Theory*, pages 186–211, 2018.
- [12] Florinel-Alin Croitoru, Vlad Hondu, Radu Tudor Ionescu, and Mubarak Shah. Diffusion models in vision: A survey. *IEEE Transactions on Pattern Analysis and Machine Intelligence*, pages 1–20, 2023. doi: 10.1109/TPAMI.2023.3261988.
- [13] Arnak S. Dalalyan and Lionel Riou-Durand. On sampling from a log-concave density using kinetic Langevin diffusions. *Bernoulli*, 26(3):1956–1988, August 2020. doi: 10.3150/19-BEJ1178.
- [14] Martin Heusel, Hubert Ramsauer, Thomas Unterthiner, Bernhard Nessler, and Sepp Hochreiter. GANs Trained by a Two Time-Scale Update Rule Converge to a Local Nash Equilibrium. In I. Guyon, U. Von Luxburg, S. Bengio, H. Wallach, R. Fergus, S. Vishwanathan, and R. Garnett, editors, *Advances in Neural Information Processing Systems*, volume 30. Curran Associates, Inc., 2017. URL https://proceedings.neurips.cc/paper_files/paper/2017/file/8a1d694707eb0fefe65871369074926d-Paper.pdf.
- [15] Jonathan Ho, Ajay Jain, and Pieter Abbeel. Denoising diffusion probabilistic models. In H. Larochelle, M. Ranzato, R. Hadsell, M.F. Balcan, and H. Lin, editors, *Advances in Neural Information Processing Systems*, volume 33, pages 6840–6851. Curran Associates, Inc., 2020. URL https://proceedings.neurips.cc/paper_files/paper/2020/file/4c5bcfec8584af0d967f1ab10179ca4b-Paper.pdf.
- [16] Chin-Wei Huang, Jae Hyun Lim, and Aaron Courville. A variational perspective on diffusion-based generative models and score matching. In A. Beygelzimer, Y. Dauphin, P. Liang, and J. Wortman Vaughan, editors, *Advances in Neural Information Processing Systems*, 2021. URL <https://openreview.net/forum?id=bXehDYUjjXi>.
- [17] Ian T. Jolliffe and Jorge Cadima. Principal component analysis: a review and recent developments. *Philosophical Transactions of the Royal Society A: Mathematical, Physical and Engineering Sciences*, 374(2065):20150202, 2016. doi: 10.1098/rsta.2015.0202.
- [18] Fima C Klebaner. *Introduction to Stochastic Calculus with Applications*. IMPERIAL COLLEGE PRESS, 1998. doi: 10.1142/p110. URL <https://www.worldscientific.com/doi/abs/10.1142/p110>.
- [19] Peter E. Kloeden and Eckhard Platen. *Numerical Solution of Stochastic Differential Equations*. Springer Berlin Heidelberg, 1992. doi: 10.1007/978-3-662-12616-5. URL <https://doi.org/10.1007/978-3-662-12616-5>.

- [20] F. Otto and C. Villani. Generalization of an Inequality by Talagrand and Links with the Logarithmic Sobolev Inequality. *Journal of Functional Analysis*, 173(2):361 – 400, 2000. ISSN 0022-1236. doi: <https://doi.org/10.1006/jfan.1999.3557>. URL <http://www.sciencedirect.com/science/article/pii/S0022123699935577>.
- [21] Jascha Sohl-Dickstein, Eric Weiss, Niru Maheswaranathan, and Surya Ganguli. Deep unsupervised learning using nonequilibrium thermodynamics. In Francis Bach and David Blei, editors, *Proceedings of the 32nd International Conference on Machine Learning*, volume 37 of *Proceedings of Machine Learning Research*, pages 2256–2265, Lille, France, 07–09 Jul 2015. PMLR.
- [22] Casper Kaae Sønderby, Jose Caballero, Lucas Theis, Wenzhe Shi, and Ferenc Huszár. Amortised MAP inference for image super-resolution. In *International Conference on Learning Representations*, 2017. URL <https://openreview.net/forum?id=S1RP6GLle>.
- [23] Jiaming Song, Chenlin Meng, and Stefano Ermon. Denoising diffusion implicit models. In *International Conference on Learning Representations*, 2021. URL <https://openreview.net/forum?id=St1giarCHLP>.
- [24] Yang Song and Stefano Ermon. Generative Modeling by Estimating Gradients of the Data Distribution. In H. Wallach, H. Larochelle, A. Beygelzimer, F. d’Alché-Buc, E. Fox, and R. Garnett, editors, *Advances in Neural Information Processing Systems*, volume 32. Curran Associates, Inc., 2019. URL https://proceedings.neurips.cc/paper_files/paper/2019/file/3001ef257407d5a371a96dcd947c7d93-Paper.pdf.
- [25] Yang Song, Jascha Sohl-Dickstein, Diederik P Kingma, Abhishek Kumar, Stefano Ermon, and Ben Poole. Score-based generative modeling through stochastic differential equations. In *International Conference on Learning Representations*, 2021. URL <https://openreview.net/forum?id=PxTIG12RRHS>.
- [26] Yang Song, Prafulla Dhariwal, Mark Chen, and Ilya Sutskever. Consistency Models, March 2023. arXiv:2303.01469 [cs, stat].
- [27] Esteban G. Tabak and Eric Vanden-Eijnden. Density estimation by dual ascent of the log-likelihood. *Communications in Mathematical Sciences*, 8(1):217–233, March 2010. ISSN 1539-6746, 1945-0796.
- [28] Pascal Vincent. A connection between score matching and denoising autoencoders. *Neural Comput.*, 23(7):1661–1674, 2011. doi: 10.1162/NECO_a_00142.
- [29] LeCun Yann. MNIST, 1998. URL <http://yann.lecun.com/exdb/mnist/>.
- [30] Qinsheng Zhang and Yongxin Chen. Fast sampling of diffusion models with exponential integrator. In *The Eleventh International Conference on Learning Representations*, 2023. URL <https://openreview.net/forum?id=Loek7hfb46P>.
- [31] Qinsheng Zhang, Molei Tao, and Yongxin Chen. gDDIM: Generalized denoising diffusion implicit models. In *The Eleventh International Conference on Learning Representations*, 2023. URL <https://openreview.net/forum?id=1hKE9qjvz->.

APPENDIX A. NOTATION CONVENTION.

TABLE 1. Summary of important quantities in this paper

Quantity	Notation	Notes
Forward process	X_t	$t = 0$: data distribution
Backward/generative process	Y_t	$t = 0$: noise distribution
Backward process with inexact score	\tilde{Y}_t	
Distribution of forward process	p_t	$p_t := \text{law}(X_t)$
Distribution of backward process	q_t	$\text{law}(Y_t) := q_t \equiv p_{T-t} \equiv p_t^\leftarrow$
Distribution of approximated backward process	\tilde{q}_t	$\tilde{q}_t := \text{law}(\tilde{Y}_t)$, $\tilde{q}_t = q_t$ when error $\epsilon = 0$
Error function of the score	$\epsilon \mathcal{E}_t^\leftarrow$	$0 \leq \epsilon \ll 1$ and $\mathcal{E}_t^\leftarrow = \mathcal{O}(1)$
The exact potential	U_t	$p_t := e^{-U_t}$
Modified potential	V_t^\leftarrow	see (9)
Normalizing constants	$Z_V := \int e^{-V}$	V is arbitrary

APPENDIX B. DISCUSSION AND PROOF FOR § 2

B.1. **Proof of (3).** We re-state the conclusion in (3) in the following lemma:

Lemma B.1. *For any function h_t^\leftarrow , if one chooses A^\leftarrow as in (3), then we have $q_t(x) = p_{T-t}(x)$ for any $t \in [0, T]$ and $x \in \mathbb{R}^d$.*

Proof. We can easily write down the Fokker-Planck equation of (1)

$$\partial_t p_t(x) = -\nabla \cdot (f_t(x)p_t(x)) + \frac{g_t^2}{2} \Delta p_t(x).$$

Since we need to ensure $q_t = p_{T-t}$, we require

$$\begin{aligned} \partial_t q_t(x) &= \nabla \cdot (f_t^\leftarrow(x)q_t(x)) - \frac{g_t^{\leftarrow 2}}{2} \Delta q_t(x) \\ &= \nabla \cdot \left(f_t^\leftarrow(x)q_t(x) - \frac{g_t^{\leftarrow 2} + h_t^{\leftarrow 2}}{2} \nabla q_t(x) \right) + \frac{h_t^{\leftarrow 2}}{2} \Delta q_t(x) \\ &= \nabla \cdot \left((f_t^\leftarrow(x) - \frac{g_t^{\leftarrow 2} + h_t^{\leftarrow 2}}{2} \nabla \log q_t(x))q_t(x) \right) + \frac{h_t^{\leftarrow 2}}{2} \Delta q_t(x) \\ &= \nabla \cdot \left((f_t^\leftarrow(x) - \frac{g_t^{\leftarrow 2} + h_t^{\leftarrow 2}}{2} \nabla \log p_t^\leftarrow(x))q_t(x) \right) + \frac{h_t^{\leftarrow 2}}{2} \Delta q_t(x) \\ &= -\nabla \cdot (A_t^\leftarrow(x)q_t(x)) + \frac{h_t^{\leftarrow 2}}{2} \Delta q_t(x), \end{aligned}$$

by noting $A_t^\leftarrow(x)$ is specified in (3). The equation is exactly the Fokker-Planck equation (2). \square

B.2. The role of g_t . The function $t \mapsto g_t$ as the diffusion coefficient in the forward Fokker-Planck equation (1) in fact serves as a role of time re-scaling as long as $g_t > 0$ for any t . Indeed, if we have an SDE in the following form (the VP-SDE in [25])

$$dX_t = -\frac{g_t^2}{2} X_t dt + g_t dW_t, \quad t \in [0, T],$$

then by introducing $\tau : \mathbb{R}^+ \rightarrow \mathbb{R}^+$ via the ODE $\tau'(t) = (g_{\tau(t)})^{-2}$, $\tau(0) = 0$, we know that $\underline{X}_t := X_{\tau(t)}$ satisfies the following SDE [18]:

$$d\underline{X}_t = -\frac{1}{2} \underline{X}_t dt + dW_t, \quad t \in [0, \theta],$$

where $\theta := \tau^{-1}(T)$ means the inverse function of τ at time T . The Brownian motion W in \underline{X}_t is not the same Brownian motion in X_t , i.e., the driven-noise in the last two equations are not the same technically; we slightly abuse the notation for the simplicity of notations. By Lem. B.1, this SDE has the backward process as follows:

$$\begin{aligned} (16) \quad d\underline{Y}_t &\stackrel{(3)}{=} \left(\frac{1}{2} \underline{Y}_t + \frac{1 + \underline{h}_t^{\leftarrow 2}}{2} \nabla \log p_t^{\leftarrow}(\underline{Y}_t) \right) dt + \underline{h}_t^{\leftarrow} dW_t \quad t \in [0, \theta] \\ &= \left(\frac{1}{2} \underline{Y}_t + \frac{1 + \underline{h}_{\theta-t}^2}{2} \nabla \log p_{\theta-t}(\underline{Y}_t) \right) dt + \underline{h}_{\theta-t} dW_t, \end{aligned}$$

where p_t is the density function of \underline{X}_t by notation conventions in § 2. By Lem. B.1, so far we know that

$$\text{law}(\underline{Y}_{\theta-t}) \stackrel{\text{Lem. B.1}}{=} \text{law}(\underline{X}_t) = \text{law}(X_{\tau(t)}).$$

Let $f_s := \theta - (\tau^{-1})(T-s)$ and $Y_s := \underline{Y}_{f_s}$, where $s \in [0, T]$. By straightforward computation, we know

$$\begin{aligned} dY_s &= f'_s \left(\frac{1}{2} \underline{Y}_{f_s} + \frac{1 + \underline{h}_{\theta-f_s}^2}{2} \nabla \log p_{\theta-f_s}(\underline{Y}_{f_s}) \right) dt + \sqrt{f'_s \underline{h}_{\theta-f_s}^2} dW_s \\ &= f'_s \left(\frac{1}{2} Y_s + \frac{1 + \underline{h}_{\theta-f_s}^2}{2} \nabla \log p_{T-s}(Y_s) \right) dt + \sqrt{f'_s \underline{h}_{\theta-f_s}^2} dW_s. \end{aligned}$$

To get the second line, we used the fact that

$$p_{\theta-f_s} = \text{law}(\underline{X}_{\theta-f_s}) = \text{law}(\underline{X}_{\tau^{-1}(T-s)}) = \text{law}(X_{T-s}) \equiv p_{T-s}.$$

By chain rules, it is easy to compute that

$$f'_s = \frac{1}{\tau'(\tau^{-1}(T-s))} = \frac{1}{(g_{T-s})^{-2}} = g_{T-s}^2 > 0.$$

Therefore, the above SDE for Y_s has the form

$$dY_s = \left(\frac{g_{T-s}^2}{2} Y_s + g_{T-s}^2 \frac{1 + \underline{h}_{\theta-f_s}^2}{2} \nabla \log p_s^{\leftarrow}(Y_s) \right) dt + g_{T-s} \underline{h}_{\theta-f_s} dW_s.$$

This matches the form in Lem. B.1 by choosing

$$h_s^{\leftarrow} = g_{T-s} \underline{h}_{\theta-f_s} \equiv g_s^{\leftarrow} \underline{h}_{\tau^{-1}(T-s)}.$$

Hence, if we simply pick $\underline{h} = c$ as a constant function in (16), it has the same effect as choosing $h_s^{\leftarrow} = cg_s^{\leftarrow}$ where $c \in \mathbb{R}^+$. The former ($\underline{h} = c$) is used in § 3 for simplicity in theoretical analysis, and the latter ($h_s^{\leftarrow} = cg_s^{\leftarrow}$) is used in numerical experiments in § 4 to match previous literature in practice (namely, a general g). **In conclusion**, the above discussion justifies the consistency of notation and set-up between our theoretical analysis and numerical experiments.

B.3. Existing analysis of sample generation quality. In practice, one simulates the following SDE:

$$(17) \quad dZ_t = \left(-f_t^\leftarrow(Z_t) + \frac{(g_t^\leftarrow)^2 + (h_t^\leftarrow)^2}{2} \mathfrak{S}_t^\leftarrow(Z_t) \right) dt + h_t^\leftarrow dW_t, \quad \text{law}(Z_0) = \mathcal{N}(0, I_d).$$

From the analysis by Chen et al. [7, Theorem 1] for the case $h^\leftarrow = g^\leftarrow$, one has

$$\text{KL}(p_0 \parallel \hat{q}) \leq \text{KL}(p_T \parallel \mathcal{N}(0, I_d)) + \mathcal{O}(T\epsilon^2) + \mathcal{O}(T^2d/N),$$

where \hat{q} is the distribution of Z_T after applying the exponential integrator to (17) and N is the number of time-discretization steps. The first term $\text{KL}(p_T \parallel \mathcal{N}(0, I_d)) \leq (\mathcal{M}_2 + d)e^{-T}$, where $\mathcal{M}_2 = \mathbb{E}_{p_0} |x|^2$ is the second moment of data distribution.

Therefore, to ensure that $\text{KL}(p_0 \parallel \hat{q}) \leq \delta$, it is sufficient to choose

$$T = \mathcal{O}(\log(\delta/(\mathcal{M}_2 + d))).$$

The time-discretization error can be eliminated by choosing $N \rightarrow \infty$. What is so far less clear in literature is the term $\mathcal{O}(T\epsilon^2)$.

B.4. Existing error bounds fail to characterize the optimal h^\leftarrow . Note that the target dynamics q_t in (2) and the approximated dynamics \tilde{q}_t in (5) only differ in the drift term. Recall that $q_T = p_0$, and to estimate $\text{KL}(p_0 \parallel \tilde{q}_T) \equiv \text{KL}(q_T \parallel \tilde{q}_T)$, we can simply estimate how the quantity $\text{KL}(q_t \parallel \tilde{q}_t)$ changes for $t \in (0, T)$. By [7, Lemma 6] (arXiv v2), for any $t \in \mathbb{R}$,

$$(18) \quad \partial_t \text{KL}(q_t \parallel \tilde{q}_t) = -\frac{h_t^{\leftarrow 2}}{2} \mathcal{J}(q_t \parallel \tilde{q}_t) + \frac{g_t^{\leftarrow 2} + h_t^{\leftarrow 2}}{2} \mathbb{E} \left[\langle -\epsilon \mathcal{E}_t^\leftarrow(Y_t), \nabla \log \frac{q_t(Y_t)}{\tilde{q}_t(Y_t)} \rangle \right],$$

where the Fisher information $\mathcal{J}(p \parallel q) := \int dp \left| \nabla \log \frac{p}{q} \right|^2$. By Cauchy-Schwarz inequality,

$$(19) \quad \begin{aligned} & \partial_t \text{KL}(q_t \parallel \tilde{q}_t) \\ & \leq -\frac{h_t^{\leftarrow 2}}{2} \mathcal{J}(q_t \parallel \tilde{q}_t) + \frac{g_t^{\leftarrow 2} + h_t^{\leftarrow 2}}{2} \left(\frac{c^2}{2} \mathbb{E} \left[\|\epsilon \mathcal{E}_t^\leftarrow(Y_t)\|^2 \right] + \frac{1}{2c^2} \mathbb{E} \left[\left\| \nabla \log \frac{q_t(Y_t)}{\tilde{q}_t(Y_t)} \right\|^2 \right] \right) \\ & = \frac{(h_t^{\leftarrow 2} + g_t^{\leftarrow 2})^2}{8h_t^{\leftarrow 2}} \epsilon^2 \mathbb{E} \left[\|\mathcal{E}_t^\leftarrow(Y_t)\|^2 \right], \end{aligned}$$

where we choose $c^2 = \frac{h_t^{\leftarrow 2} + g_t^{\leftarrow 2}}{2h_t^{\leftarrow 2}}$ herein. This bound captures the scaling extremely well when $h^\leftarrow = g^\leftarrow$, which helps to establish the effectiveness of score-based diffusion method in [7]. However, this bound is not directly applicable for a general h^\leftarrow , as it is clear that this bound fails to provide useful information when $h^\leftarrow \approx 0$ (namely, the probability flow), as well as the large diffusion case ($h^\leftarrow \rightarrow \infty$). From directly optimizing the upper bound, i.e., minimizing $\frac{(h_t^{\leftarrow 2} + g_t^{\leftarrow 2})^2}{8h_t^{\leftarrow 2}}$, one ends up with the choice $h^\leftarrow = g^\leftarrow$, which has been used in many literature. We acknowledge that this is an effective choice; however, as we show in § 4, this is not really the optimal case in general, and the above argument cannot justify choosing the diffusion model over the probability flow.

APPENDIX C. DISCUSSION FOR § 3 AND PROOF OF PROP. 3.2

C.1. The operator $\Phi_{s,t}^{(h^\leftarrow)}$.

Lemma C.1.

- $\Phi_{(\cdot),(\cdot)}^{(h^\leftarrow)}$ satisfies the semi-group property, i.e., for any s, t, r ,

$$(20) \quad \Phi_{t,r}^{(h^\leftarrow)} \circ \Phi_{s,t}^{(h^\leftarrow)} = \Phi_{s,r}^{(h^\leftarrow)}.$$

Moreover, $\Phi_{t,t}^{(h^\leftarrow)} = \text{Id}$ is an identity operator for any t .

- For any s, t ,

$$(21) \quad \partial_s(\Phi_{s,t}^{(h^\leftarrow)}(\mu)) = -\Phi_{s,t}^{(h^\leftarrow)}(\mathcal{L}_s^{(h^\leftarrow)}\mu) \quad \partial_t(\Phi_{s,t}^{(h^\leftarrow)}(\mu)) = \mathcal{L}_t^{(h^\leftarrow)}(\Phi_{s,t}^{(h^\leftarrow)}(\mu)).$$

Proof. The semi-group structure is easy to imagine and is thus omitted herein. Next, we shall only prove the first result in (21) for illustration:

$$\begin{aligned} \partial_s(\Phi_{s,t}^{(h^\leftarrow)}(\mu)) &= \lim_{\delta s \rightarrow 0^+} \frac{\Phi_{s+\delta s,t}^{(h^\leftarrow)}(\mu) - \Phi_{s,t}^{(h^\leftarrow)}(\mu)}{\delta s} \\ &\stackrel{(20)}{=} \lim_{\delta s \rightarrow 0^+} \frac{\Phi_{s,t}^{(h^\leftarrow)}\Phi_{s+\delta s,s}^{(h^\leftarrow)}(\mu) - \Phi_{s,t}^{(h^\leftarrow)}(\mu)}{\delta s} \\ &= \lim_{\delta s \rightarrow 0^+} \frac{\Phi_{s,t}^{(h^\leftarrow)}(\Phi_{s+\delta s,s}^{(h^\leftarrow)} - \text{Id})(\mu)}{\delta s} \\ &= \lim_{\delta s \rightarrow 0^+} \frac{\Phi_{s,t}^{(h^\leftarrow)}(\text{Id} - \delta s \mathcal{L}_s^{(h^\leftarrow)} - \text{Id})(\mu)}{\delta s} \\ &= -\Phi_{s,t}^{(h^\leftarrow)}(\mathcal{L}_s^{(h^\leftarrow)}(\mu)). \end{aligned}$$

□

Lemma C.2. Suppose $(t, x) \mapsto \mu_t(x)$, $(t, x) \mapsto \theta_t(x)$ are time-dependent functions. Suppose $\partial_t \mu_t = \mathcal{L}_t^{(h^\leftarrow)}(\mu_t) + \theta_t$ with $\mu_0 = 0$, then

$$\mu_T = \int_0^T \Phi_{t,T}^{(h^\leftarrow)}(\theta_t) dt.$$

Proof. Note that

$$\partial_t(\Phi_{t,0}^{(h^\leftarrow)}\mu_t) \stackrel{(21)}{=} \Phi_{t,0}^{(h^\leftarrow)}(-\mathcal{L}_t^{(h^\leftarrow)}\mu_t) + \Phi_{t,0}^{(h^\leftarrow)}(\mathcal{L}_t^{(h^\leftarrow)}\mu_t + \theta_t) = \Phi_{t,0}^{(h^\leftarrow)}(\theta_t).$$

Therefore,

$$\Phi_{T,0}^{(h^\leftarrow)}(\mu_T) = \int_0^T \Phi_{t,0}^{(h^\leftarrow)}(\theta_t) dt.$$

By applying the operator $\Phi_{0,T}^{(h^\leftarrow)}$ to both sides, we have

$$\mu_T = \int_0^T \Phi_{0,T}^{(h^\leftarrow)} \circ \Phi_{t,0}^{(h^\leftarrow)}(\theta_t) dt \stackrel{(20)}{=} \int_0^T \Phi_{t,T}^{(h^\leftarrow)}(\theta_t) dt.$$

□

C.2. Time re-scaling of $\mathcal{L}^{(h^\leftarrow)}$ and connections to almost quasi-static Langevin process. By time re-scaling, it is immediate to obtain the following result:

Lemma C.3. *Suppose $h_t^\leftarrow = h$ for any $t \in [0, T]$ for simplicity. For any probability distribution μ , the probability distribution $\Phi_{s,t}^{(h^\leftarrow)}(\mu)$ (with $s < t$) is the final state of the following PDE on the time interval $\tilde{r} \in [0, (t-s)h^2/2]$:*

$$(22) \quad \partial_{\tilde{r}} \tilde{\mu}_{\tilde{r}} = \Delta \tilde{\mu}_{\tilde{r}} + \nabla \cdot \left(\nabla V_{s+2\tilde{r}/h^2}^\leftarrow \tilde{\mu}_{\tilde{r}} \right), \quad \tilde{\mu}_0 = \mu.$$

It corresponds to the following Langevin with time-dependent potential:

$$dX_{\tilde{r}} = -\nabla V_{s+2\tilde{r}/h^2}^\leftarrow(X_{\tilde{r}}) d\tilde{r} + \sqrt{2} dW_{\tilde{r}}, \quad \text{law}(X_0) = \mu.$$

Proof. To obtain $\Phi_{s,t}^{(h^\leftarrow)}(\mu)$, we simply solve the following PDE:

$$\partial_r \mu_r \stackrel{(9)}{=} \frac{h^2}{2} (\Delta \mu_r + \nabla \cdot (\nabla V_r^\leftarrow \mu_r)) \quad \mu_s = \mu.$$

By change of variables $\tilde{r} = (r-s)h^2/2$ and $\tilde{\mu}_{\tilde{r}} := \mu_r \equiv \mu_{s+2\tilde{r}/h^2}$, we immediately have (22), and the corresponding Langevin dynamics easily follows. \square

When $h \rightarrow \infty$, the potential in the Langevin dynamics $\tilde{r} \mapsto V_{s+2\tilde{r}/h^2}^\leftarrow$ evolves extremely slowly. From (9), we also know that $V_{s+2\tilde{r}/h^2}^\leftarrow \approx U_s^\leftarrow$ when $\tilde{r} = 0$ and is approximately U_t^\leftarrow when $\tilde{r} = \frac{(t-s)h^2}{2}$. Therefore, the Langevin dynamics can be viewed as an almost *quasi-static process* [6] approximately transforming the state p_s^\leftarrow to the state p_t^\leftarrow over an extremely long time period though.

C.3. Proof of Prop. 3.2.

Denote

$$v_t(x) := \partial_\epsilon q_t^\epsilon(x)|_{\epsilon=0}, \quad \zeta_t(x) := \partial_\epsilon^2 q_t^\epsilon(x)|_{\epsilon=0}.$$

Namely, we expand \tilde{q}_t^ϵ via the following

$$\tilde{q}_t^\epsilon(x) = \underbrace{\tilde{q}_t^0(x)}_{\equiv q_t(x)} + \epsilon v_t(x) + \frac{\epsilon^2}{2} \zeta_t(x) + \mathcal{O}(\epsilon^3).$$

Recall that when $\epsilon = 0$, $\tilde{q}_t^0 \equiv q_t$; in particular, $\tilde{q}_T^0 = q_T \stackrel{\text{Lem. B.1}}{=} p_0$. The cost function can be easily expanded via Taylor's formula:

$$\text{KL}(p_0 || \tilde{q}_T^\epsilon) = -\epsilon \int_{\mathbb{R}^d} v_T(x) dx - \frac{\epsilon^2}{2} \int_{\mathbb{R}^d} \left(\zeta_T(x) - \frac{v_T^2(x)}{p_0(x)} \right) dx + \mathcal{O}(\epsilon^3).$$

Since $\int \tilde{q}_T^\epsilon \equiv 1$, it is easy to know that $\int v_T = \int \zeta_T = 0$ and thus

$$\text{KL}(p_0 || \tilde{q}_T^\epsilon) = \frac{\epsilon^2}{2} \int_{\mathbb{R}^d} \frac{v_T^2(x)}{p_0(x)} dx + \mathcal{O}(\epsilon^3).$$

Next we need to study v_T . Recall from (5) that the Fokker-Planck equation of \tilde{q}_t is

$$\partial_t \tilde{q}_t^\epsilon = \mathcal{L}_t^{(h^\leftarrow)}(\tilde{q}_t^\epsilon) - \epsilon \nabla \cdot \left(\frac{1 + h_t^{\leftarrow 2}}{2} \mathcal{E}_t^\leftarrow \tilde{q}_t^\epsilon \right).$$

By taking derivatives with respect to ϵ on both sides of this equation and then passing $\epsilon \rightarrow 0$, we know that

$$\partial_t v_t = \mathcal{L}_t^{(h^\leftarrow)}(v_t) - \nabla \cdot \left(\frac{1 + h_t^{\leftarrow 2}}{2} \mathcal{E}_t^\leftarrow q_t \right).$$

By Lem. C.2,

$$(23) \quad v_T = -\frac{1}{2} \int_0^T (1 + h_t^{(h)}) \Phi_{t,T}^{(h)} \left(\nabla \cdot \left(\underbrace{q_t}_{\equiv p_t^{(h)}} \mathcal{E}_t^{(h)} \right) \right) dt.$$

APPENDIX D. PRELIMINARY RESULTS

We collect two lemmas which will be useful in proving Prop. 3.5 and Prop. 3.6 later.

Lemma D.1.

- (1) *The operator $\mathcal{K}(f) := \Delta f + \nabla \cdot (\nabla V \cdot f)$ is a Hermitian/self-adjoint operator in the space $\langle \cdot, \cdot \rangle_{L^2(\rho^{-1})}$ where $\rho \propto e^{-V}$. Therefore, \mathcal{K} has the eigen-decomposition in this weighted $L^2(\rho^{-1})$ space.*
- (2) *Assume that $\nabla^2 V(x) \geq m \mathbf{I}_d$ for any $x \in \mathbb{R}^d$ for some $m > 0$. Then the operator $-\mathcal{K}$ is a positive operator on the space $\{f : \int f = 0\}$ with spectrum gap at least m .*

Proof. For any f, g , note that

$$\langle f, \mathcal{K}g \rangle_{L^2(\rho^{-1})} = - \int_{\mathbb{R}^d} \nabla(f/\rho) \cdot \nabla(g/\rho) \rho.$$

Therefore, \mathcal{K} is a Hermitian operator. In the space $\{f : \int f = 0\}$, we know

$$\begin{aligned} -\langle f, \mathcal{K}f \rangle_{L^2(\rho^{-1})} &= \int_{\mathbb{R}^d} |\nabla(f/\rho)|^2 \rho \\ &\stackrel{\text{Poincaré ineq.}}{\geq} m \int_{\mathbb{R}^d} (f^2/\rho^2) \rho = m \langle f, f \rangle_{L^2(\rho^{-1})}. \end{aligned}$$

The validity of Poincaré inequality under the strong convexity assumption is well-known in literature; see, e.g., [2, 20] and [3, Corollary 4.8.2]. \square

Lemma D.2. *Suppose the operator \mathcal{K} is defined as $\mathcal{K}(f) := \Delta f + \nabla \cdot (\nabla V \cdot f)$ with $\nabla^2 V(x) \geq m \mathbf{I}_d$ for any $x \in \mathbb{R}^d$. Then for any $c, a \in \mathbb{R}^+$, and any function φ with $\int \varphi = 0$,*

$$\begin{aligned} \int_{\mathbb{R}^d} \frac{1}{\rho} \left(\int_0^a \exp(ct\mathcal{K})(\varphi) dt \right)^2 &= \sum_{k=1}^{\infty} \left(\frac{1 - e^{-ac\lambda_k}}{c\lambda_k} \right)^2 \alpha_k^2 \\ &\leq \left(\frac{1 - e^{-acm}}{cm} \right)^2 \int_{\mathbb{R}^d} \frac{\varphi^2}{\rho}, \end{aligned}$$

where $\rho \propto e^{-V}$, $\{(\lambda_k, \phi_k)\}_{k=1}^{\infty}$ are eigen pairs for the operator $-\mathcal{K}$, and $\varphi = \sum_{k=1}^{\infty} \alpha_k \phi_k$.

Remark. Note that as \mathcal{K} is an operator, $\exp(ct\mathcal{K}) := \sum_{k=0}^{\infty} \frac{(ct\mathcal{K})^k}{k!}$ is the operator exponential.

Proof. Let us first denote the eigenvalue decomposition of \mathcal{K} as $\mathcal{K}(\phi_k) = -\lambda_k \phi_k$ where $\lambda_k \geq m$ for $k \in \mathbb{N}$ and $\langle \phi_j, \phi_k \rangle_{L^2(\rho^{-1})} = \delta_{j,k}$ for any $j, k \in \mathbb{N}$ by Lem. D.1. Then we can decompose φ by $\varphi = \sum_k \alpha_k \phi_k$. It is not hard to verify that

$$\exp(ct\mathcal{K})(\varphi) = \sum_{k=1}^{\infty} e^{-ct\lambda_k} \alpha_k \phi_k.$$

Then

$$\int_0^a \exp(ct\mathcal{K})(\varphi) dt = \sum_{k=1}^{\infty} \frac{1 - e^{-ac\lambda_k}}{c\lambda_k} \alpha_k \phi_k.$$

Hence,

$$\begin{aligned} \int_{\mathbb{R}^d} \frac{1}{\rho} \left(\int_0^a \exp(ct\mathcal{K})(\varphi) dt \right)^2 dt &= \int_{\mathbb{R}^d} \frac{1}{\rho} \left(\sum_{k=1}^{\infty} \frac{1 - e^{-ac\lambda_k}}{c\lambda_k} \alpha_k \phi_k \right)^2 dt \\ &= \sum_{k=1}^{\infty} \left(\frac{1 - e^{-ac\lambda_k}}{c\lambda_k} \right)^2 \alpha_k^2 \\ &\leq \left(\frac{1 - e^{-acm}}{cm} \right)^2 \sum_{k=1}^{\infty} \alpha_k^2 \\ &= \left(\frac{1 - e^{-acm}}{cm} \right)^2 \int_{\mathbb{R}^d} \frac{\varphi^2}{\rho} dt. \end{aligned}$$

□

APPENDIX E. PROOF OF PROP. 3.4

For convenience, we summarize some notations below; see also Appx. A.

- Denote the global minimum of U_t^\leftarrow as \mathcal{X}_t^\leftarrow and denote the global minimum of V_t^\leftarrow as \mathcal{Y}_t^\leftarrow . When $h \rightarrow \infty$, we know

$$\lim_{h \rightarrow \infty} \mathcal{Y}_t \rightarrow \mathcal{X}_t.$$

- Denote the normalizing constant $Z_V := \int e^{-V}$ for an arbitrary potential V .
- Recall that the distribution of the exact dynamics Y_t is $q_t \equiv p_{T-t} \equiv p_t^\leftarrow$ and the distribution of the approximated dynamics \tilde{Y}_t is \tilde{q}_t .
- Recall that $p_t := e^{-U_t}$ and $\rho_t \propto e^{-V_t}$ in (10).

Lemma E.1. *Under Assumption 3.3, we have:*

- (i) *Assumption 3.1 (3) is valid, i.e., the existence of c_U .*
- (ii) *For any $t \in [0, T]$, the probability distribution ρ_t defined in (10) satisfies the Poincaré inequality with constant κ_t (14):*

$$(24) \quad \int_{\mathbb{R}^d} |\nabla \varphi|^2 d\rho_t \geq \kappa_t \int_{\mathbb{R}^d} \varphi^2 d\rho_t, \quad \forall \varphi \text{ with } \int_{\mathbb{R}^d} \varphi \rho_t = 0.$$

- (iii) *$Z_{V_0} := \int_{\mathbb{R}^d} e^{-V_0}$ is both upper and lower bounded: for any $\delta \in (0, 1)$, there exists $h_0(\delta) > 0$ such that whenever $h \geq h_0(\delta)$,*

$$1 - \delta \leq Z_{V_0} \leq e^{-h^{-2}c_U}.$$

and

$$\frac{\rho_0}{p_0} \leq \frac{e^{-h^{-2}c_U}}{1 - \delta}.$$

(iv) If we pick $\delta = 1/2$, for $h \geq \max\{h_0(1/2), \sqrt{\max\{0, -\frac{c_U}{\ln(2)}\}}\}$, the function ρ_0/p_0 is uniformly bounded:

$$(25) \quad \frac{\rho_0}{p_0} \leq 4.$$

Proposition E.2. For any $h \geq 1/2$, we have

$$\left| \int_{\mathbb{R}^d} \varphi^2 \frac{d}{dt} \rho_t^\leftarrow \right| \leq C_t^{\leftarrow, (1)} \int_{\mathbb{R}^d} \varphi^2 \rho_t^\leftarrow + C_t^{\leftarrow, (2)} \int_{\mathbb{R}^d} |\nabla \varphi|^2 \rho_t^\leftarrow, \quad \forall \varphi \in C_0^2(\mathbb{R}^d).$$

where

$$(26) \quad \begin{cases} C_t^{\leftarrow, (1)} := \xi_t^\leftarrow + 2\xi_t^\leftarrow |\mathcal{Y}_t^\leftarrow - \mathcal{X}_t^\leftarrow|^2 + \frac{20dM_t^{\leftarrow-2}\xi_t^\leftarrow}{m_t^{\leftarrow-2}}, \\ C_t^{\leftarrow, (2)} := \frac{8\xi_t^\leftarrow}{m_t^{\leftarrow-2}} \equiv \frac{20 + 30M_t^{\leftarrow-2}}{m_t^{\leftarrow-2}}, \\ \xi_t^\leftarrow := |\partial_t \log Z_{V_t^\leftarrow}| + \frac{5d(1 + M_t^{\leftarrow-2})}{2} + \frac{5}{2}|\mathcal{X}_t^\leftarrow|^2, \\ \varsigma_t^\leftarrow := 5\left(\frac{1}{2} + \frac{3M_t^{\leftarrow-2}}{4}\right). \end{cases}$$

$Z_{V_t^\leftarrow} = \int e^{-V_t^\leftarrow}$, M_t^\leftarrow and m_t^\leftarrow are shown in [Assumption 3.3](#), and \mathcal{X}_t^\leftarrow and \mathcal{Y}_t^\leftarrow are the global minimum points of functions $x \mapsto U_t^\leftarrow(x)$ and $x \mapsto V_t^\leftarrow(x)$, respectively.

Remark. A similar result holds for any $h > 0$; we choose $h \geq 1/2$ in order to simplify the above constants (26).

Note that the constant $C_t^{\leftarrow, (2)}$ is independent of h . We remark that when $h \gg 1$, $C_t^{\leftarrow, (1)}$ approximately behaves as follows:

Lemma E.3. When $h \rightarrow \infty$, we have

$$\lim_{h \rightarrow \infty} C_t^{\leftarrow, (1)} = \frac{5d(1 + M_t^{\leftarrow-2})}{2} + \frac{5}{2}|\mathcal{X}_t^\leftarrow|^2 + \frac{(50 + 75M_t^{\leftarrow-2})dM_t^{\leftarrow-2}}{m_t^{\leftarrow-2}}.$$

We now proceed to finish the proof of [Prop. 3.4](#). The detailed proofs of [Lem. E.1](#), [Prop. E.2](#), and [Lem. E.3](#) are postponed to [Appx. E.1](#).

Proof of Prop. 3.4. By [Lem. E.1](#),

$$(27) \quad \begin{aligned} L(h) &\stackrel{(11)}{=} \frac{(1 + h^2)^2}{8} \int_{\mathbb{R}^d} \frac{\left(\Phi_{s,T}^{(h^\leftarrow)}(\nabla \cdot (p_s^\leftarrow E))\right)^2}{\rho_0} \frac{\rho_0}{p_0} \\ &\stackrel{(25)}{\leq} \frac{1}{2}(1 + h^2)^2 \int_{\mathbb{R}^d} \frac{\left(\Phi_{s,T}^{(h^\leftarrow)}(\nabla \cdot (p_s^\leftarrow E))\right)^2}{\rho_0}. \end{aligned}$$

To simplify notations, let

$$\Lambda_t^\leftarrow := \Phi_{s,t}^{(h^\leftarrow)}(\nabla \cdot (p_s^\leftarrow E)), \quad J(h, t) := \int_{\mathbb{R}^d} \frac{\Lambda_t^{\leftarrow-2}}{\rho_t^\leftarrow}, \quad t \in [s, T].$$

After taking the time-derivative and using Lemma C.1 (in the first line below), and expressions (9) in the second line below, and integration by parts in the third line, the expression of ρ_t^{\leftarrow} (10) in the fourth line, we have

$$\begin{aligned}
\frac{d}{dt} J(h, t) &= 2 \int_{\mathbb{R}^d} \frac{\Lambda_t^{\leftarrow} \mathcal{L}_t^{(h^{\leftarrow})}(\Lambda_t^{\leftarrow})}{\rho_t^{\leftarrow}} - \int_{\mathbb{R}^d} \frac{\Lambda_t^{\leftarrow 2}}{(\rho_t^{\leftarrow})^2} \frac{d}{dt} \rho_t^{\leftarrow} \\
&= h^2 \int_{\mathbb{R}^d} \frac{\Lambda_t^{\leftarrow}}{\rho_t^{\leftarrow}} (\Delta \Lambda_t^{\leftarrow} + \nabla \cdot (\nabla V_t^{\leftarrow} \Lambda_t^{\leftarrow})) - \int_{\mathbb{R}^d} \frac{\Lambda_t^{\leftarrow 2}}{(\rho_t^{\leftarrow})^2} \frac{d}{dt} \rho_t^{\leftarrow} \\
(28) \quad &= -h^2 \int_{\mathbb{R}^d} \nabla \frac{\Lambda_t^{\leftarrow}}{\rho_t^{\leftarrow}} \cdot (\nabla \Lambda_t^{\leftarrow} + \nabla V_t^{\leftarrow} \Lambda_t^{\leftarrow}) - \int_{\mathbb{R}^d} \frac{\Lambda_t^{\leftarrow 2}}{(\rho_t^{\leftarrow})^2} \frac{d}{dt} \rho_t^{\leftarrow} \\
&= -h^2 \int_{\mathbb{R}^d} \left| \nabla \frac{\Lambda_t^{\leftarrow}}{\rho_t^{\leftarrow}} \right|^2 \rho_t^{\leftarrow} - \int_{\mathbb{R}^d} \frac{\Lambda_t^{\leftarrow 2}}{(\rho_t^{\leftarrow})^2} \frac{d}{dt} \rho_t^{\leftarrow}.
\end{aligned}$$

The major challenge is to estimate $\int_{\mathbb{R}^d} \frac{\Lambda_t^{\leftarrow 2}}{(\rho_t^{\leftarrow})^2} \frac{d}{dt} \rho_t^{\leftarrow}$. By Prop. E.2,

$$\begin{aligned}
\frac{d}{dt} J(h, t) &\leq - (h^2 - C_t^{\leftarrow, (2)}) \int_{\mathbb{R}^d} \left| \nabla \frac{\Lambda_t^{\leftarrow}}{\rho_t^{\leftarrow}} \right|^2 d\rho_t^{\leftarrow} + C_t^{\leftarrow, (1)} \int_{\mathbb{R}^d} \left(\frac{\Lambda_t^{\leftarrow}}{\rho_t^{\leftarrow}} \right)^2 d\rho_t^{\leftarrow} \\
&\stackrel{(24)}{\leq} (- (h^2 - C_t^{\leftarrow, (2)}) \kappa_t^{\leftarrow} + C_t^{\leftarrow, (1)}) \int_{\mathbb{R}^d} \left(\frac{\Lambda_t^{\leftarrow}}{\rho_t^{\leftarrow}} \right)^2 d\rho_t^{\leftarrow}.
\end{aligned}$$

Note that we need $h^2 - C_t^{\leftarrow, (2)} \geq 0$ in order to ensure the correct direction when applying the Poincaré inequality above, which explains the lower bound that h needs to satisfy in Prop. 3.4.

By Gröwnwall's inequality, for any $t \geq s$,

$$(29) \quad J(h, t) \leq J(h, s) \exp \left(- \int_s^t ((h^2 - C_r^{\leftarrow, (2)}) \kappa_r^{\leftarrow} - C_r^{\leftarrow, (1)}) dr \right).$$

Finally, by (27), we have

$$L(h) \leq C_h (1 + h^2)^2 \exp \left(- \int_s^T ((h^2 - C_r^{\leftarrow, (2)}) \kappa_r^{\leftarrow} - C_r^{\leftarrow, (1)}) dr \right),$$

where

$$(30) \quad C_h = \frac{1}{2} J(h, s) = \frac{1}{2} \int_{\mathbb{R}^d} \frac{(\nabla \cdot (p_s^{\leftarrow} E))^2}{\rho_s^{\leftarrow}}.$$

Recall that $C_t^{\leftarrow, (2)}$ (26) is independent of h . By Lem. E.3, we already discussed that $\lim_{h \rightarrow \infty} C_t^{\leftarrow, (1)}$ exists. When $h \rightarrow \infty$, we know that $\rho_s^{\leftarrow} \rightarrow p_s^{\leftarrow}$ (9)(10), and thus,

$$\lim_{h \rightarrow \infty} C_h = \frac{1}{2} \int_{\mathbb{R}^d} \frac{(\nabla \cdot (p_s^{\leftarrow} E))^2}{p_s^{\leftarrow}}.$$

This completes the proof of Prop. 3.4. \square

E.1. Proof of Lem. E.1, Prop. E.2, and Lem. E.3.

Proof of Lem. E.1. (i) From $m_0 > 1$ in **Assumption 3.3**, $x \mapsto U_0(x) - x^2/2$ is strongly convex and thus is surely bounded from below by some $c_U \in \mathbb{R}$.

(ii) The second result is a classical result by Bakry-Emery criterion [2, 3], as V_t^\leftarrow (10) is strongly convex with Hessian lower bound κ_t^\leftarrow (14).

(iii) To prove the third one, note that

$$\begin{aligned} Z_{V_0} &:= \int_{\mathbb{R}^d} e^{-V_0} \stackrel{(10)}{=} \int_{\mathbb{R}^d} e^{-(1+\hbar^{-2})U_0(x) + \hbar^{-2}|x|^2/2} dx \\ &= \int_{\mathbb{R}^d} e^{-U_0(x)} e^{-\hbar^{-2}(U_0(x) - |x|^2/2)} dx \\ &\leq e^{-\hbar^{-2}c_U} \int_{\mathbb{R}^d} e^{-U_0} = e^{-\hbar^{-2}c_U}. \end{aligned}$$

To prove the lower bound,

$$(31) \quad Z_{V_0} \geq \int_{\mathbb{R}^d} e^{-(1+\hbar^{-2})U_0(x)} dx = e^{-(1+\hbar^{-2})U_0(\mathcal{X}_0)} \int_{\mathbb{R}^d} e^{-(1+\hbar^{-2})(U_0(x) - U_0(\mathcal{X}_0))} dx.$$

Recall from the beginning of this Appendix, \mathcal{X}_0 is defined as the global minimum of $x \mapsto U_0(x)$. Then, $U_0(x) \geq U_0(\mathcal{X}_0)$ for any x and we know $\hbar \mapsto e^{-(1+\hbar^{-2})(U_0(x) - U_0(\mathcal{X}_0))}$ is monotone increasing. By monotone convergence theorem,

$$\begin{aligned} \lim_{\hbar \rightarrow \infty} \int_{\mathbb{R}^d} e^{-(1+\hbar^{-2})(U_0(x) - U_0(\mathcal{X}_0))} dx &= \int_{\mathbb{R}^d} \lim_{\hbar \rightarrow \infty} e^{-(1+\hbar^{-2})(U_0(x) - U_0(\mathcal{X}_0))} dx \\ &= \int_{\mathbb{R}^d} e^{-U_0(x) + U_0(\mathcal{X}_0)} dx = e^{U_0(\mathcal{X}_0)}. \end{aligned}$$

Thus, the limit of the right-hand side of (31) is 1 when $\hbar \rightarrow \infty$. Hence, the lower bound of Z_{V_0} follows immediately. Finally, when $\hbar \geq \hbar_0(\delta)$,

$$(32) \quad \frac{\rho_0}{p_0}(x) = \frac{e^{-(1+\hbar^{-2})U_0(x) + \hbar^{-2}|x|^2/2}}{Z_{V_0} e^{-U_0}} \leq \frac{e^{-\hbar^{-2}c_U}}{1 - \delta}.$$

(iv) When we pick $\delta = 1/2$ and choose \hbar as specified, we can immediately obtain (25). \square

Before we prove Prop. E.2, we need the following three lemmas.

Lemma E.4. *Under Assumption 3.3, we have*

$$|\partial_t U_t(x)| \leq \frac{d(1 + M_t)}{2} + \frac{|x|^2}{4} + \frac{3M_t^2}{4}|x - \mathcal{X}_t|^2.$$

Proof. Since p_t follows the Fokker-Planck equation $\partial_t p_t = \nabla \cdot (\frac{1}{2}xp_t) + \frac{1}{2}\Delta p_t$, then $U_t = -\log p_t$ satisfies $\partial_t U_t(x) = -\frac{1}{2}(d - x \cdot \nabla U_t(x) - \Delta U_t(x) + |\nabla U_t(x)|^2)$. Then by **Assumption 3.3**,

$$\begin{aligned} |\partial_t U_t(x)| &\leq \frac{d}{2} + \frac{1}{2}|x \cdot \nabla U_t(x)| + \frac{1}{2}\Delta U_t(x) + \frac{1}{2}|\nabla U_t(x)|^2 \quad (\text{triangle inequality}) \\ &\leq \frac{d}{2} + \frac{1}{4}(|x|^2 + |\nabla U_t(x)|^2) + \frac{1}{2}\Delta U_t(x) + \frac{1}{2}|\nabla U_t(x)|^2 \quad (\text{Cauchy inequality}) \\ &\leq \frac{d}{2} + \frac{1}{4}|x|^2 + \frac{3}{4}|\nabla U_t(x) - \nabla U_t(\mathcal{X}_t)|^2 + \frac{dM_t}{2} \quad (\text{by } \nabla U_t(\mathcal{X}_t) \equiv 0) \\ &\leq \frac{d(1+M_t)}{2} + \frac{|x|^2}{4} + \frac{3M_t^2}{4}|x - \mathcal{X}_t|^2. \end{aligned}$$

Recall that \mathcal{X}_t is defined as the global minimum of U_t and thus $\nabla U_t(\mathcal{X}_t) = 0$. \square

Lemma E.5. *When $\mathsf{h} \geq \frac{1}{2}$,*

$$(33) \quad \frac{|\frac{d}{dt} \rho_t^\leftarrow|}{\rho_t^\leftarrow}(x) \leq \xi_t^\leftarrow + \varsigma_t^\leftarrow |x - \mathcal{X}_t^\leftarrow|^2,$$

where

$$\begin{cases} \xi_t^\leftarrow := |\partial_t \log Z_{V_t^\leftarrow}| + \frac{5d(1+M_t^\leftarrow)}{2} + \frac{5}{2}|\mathcal{X}_t^\leftarrow|^2, \\ \varsigma_t^\leftarrow := 5\left(\frac{1}{2} + \frac{3M_t^{\leftarrow-2}}{4}\right). \end{cases}$$

Proof. By direct calculation from the definitions of ρ_t^\leftarrow in (10) and V_t^\leftarrow in (9),

$$\partial_t \rho_t^\leftarrow = -(\partial_t \log Z_{V_t^\leftarrow}) \rho_t^\leftarrow - (1 + \mathsf{h}^{-2}) \rho_t^\leftarrow \partial_t U_t^\leftarrow.$$

Hence, by Lem. E.4 and $\mathsf{h} \geq \frac{1}{2}$,

$$\begin{aligned} \frac{|\partial_t \rho_t^\leftarrow|}{\rho_t^\leftarrow}(x) &\leq |\partial_t \log Z_{V_t^\leftarrow}| + (1 + \mathsf{h}^{-2})\left(\frac{d(1+M_t^\leftarrow)}{2} + \frac{|x|^2}{4} + \frac{3M_t^{\leftarrow-2}}{4}|x - \mathcal{X}_t^\leftarrow|^2\right) \\ &\leq \left(|\partial_t \log Z_{V_t^\leftarrow}| + \frac{5d(1+M_t^\leftarrow)}{2}\right) \\ &\quad + 5\left(\frac{|\mathcal{X}_t^\leftarrow|^2}{2} + \frac{|x - \mathcal{X}_t^\leftarrow|^2}{2} + \frac{3M_t^{\leftarrow-2}}{4}|x - \mathcal{X}_t^\leftarrow|^2\right) \\ &= \xi_t^\leftarrow + 5\left(\frac{1}{2} + \frac{3M_t^{\leftarrow-2}}{4}\right)|x - \mathcal{X}_t^\leftarrow|^2. \end{aligned}$$

\square

Lemma E.6. *Assume that $\rho \propto e^{-V}$ and φ decays fast enough such that*

$$\int_{B_0(R)} \nabla \cdot (\varphi^2 \nabla \rho) \rightarrow 0,$$

as the radius $R \rightarrow \infty$ ($B_0(R)$ is the ball centered at 0 with radius R), e.g., $\varphi \in C_0^2(\mathbb{R}^d)$. Then

$$(34) \quad \int_{\mathbb{R}^d} |\nabla V|^2 \varphi^2 \rho \leq 4 \int_{\mathbb{R}^d} |\nabla \varphi|^2 \rho + 2 \int_{\mathbb{R}^d} \varphi^2 \Delta V \rho.$$

Proof. The identity $\nabla \cdot (\varphi^2 \nabla \rho) = \nabla \varphi^2 \cdot \nabla \rho + \varphi^2 \Delta \rho$ and the trivial facts $\nabla \rho = -\rho \nabla V$, $\Delta \rho = (|\nabla V|^2 - \Delta V)\rho$ show that

$$\begin{aligned} 0 &= \int \nabla \varphi^2 \cdot \nabla \rho + \varphi^2 \Delta \rho \\ &= -2 \int (\nabla V \cdot \nabla \varphi) \varphi \rho + \int \varphi^2 (-\Delta V + |\nabla V|^2) \rho \\ &\stackrel{\text{Cauchy ineq1}}{\geq} -\frac{1}{2} \int |\nabla V|^2 \varphi^2 \rho - 2 \int |\nabla \varphi|^2 \rho - \int \varphi^2 \Delta V \rho + \int |\nabla V|^2 \varphi^2 \rho \\ &= \frac{1}{2} \int |\nabla V|^2 \varphi^2 \rho - 2 \int |\nabla \varphi|^2 \rho - \int \varphi^2 \Delta V \rho. \end{aligned}$$

Therefore,

$$\int |\nabla V|^2 \varphi^2 \rho \leq 4 \int |\nabla \varphi|^2 \rho + 2 \int \varphi^2 \Delta V \rho.$$

□

Proof of Prop. E.2. The above three lemmas show that

$$\begin{aligned} &\left| \int_{\mathbb{R}^d} \varphi^2 \frac{d}{dt} \rho_t^\leftarrow \right| \stackrel{(33)}{\leq} \int_{\mathbb{R}^d} \varphi^2 (\xi_t^\leftarrow + \varsigma_t^\leftarrow |x - \mathcal{X}_t^\leftarrow|^2) \rho_t^\leftarrow \\ &= \xi_t^\leftarrow \int_{\mathbb{R}^d} \varphi^2 \rho_t^\leftarrow + \varsigma_t^\leftarrow \int_{\mathbb{R}^d} \varphi^2 |x - \mathcal{Y}_t^\leftarrow + \mathcal{Y}_t^\leftarrow - \mathcal{X}_t^\leftarrow|^2 \rho_t^\leftarrow \\ &\stackrel{\text{Cauchy ineq.}}{\leq} (\xi_t^\leftarrow + 2\varsigma_t^\leftarrow |\mathcal{Y}_t^\leftarrow - \mathcal{X}_t^\leftarrow|^2) \int_{\mathbb{R}^d} \varphi^2 \rho_t^\leftarrow + 2\varsigma_t^\leftarrow \int_{\mathbb{R}^d} \varphi^2 |x - \mathcal{Y}_t^\leftarrow|^2 \rho_t^\leftarrow \\ &\stackrel{(12)}{\leq} (\xi_t^\leftarrow + 2\varsigma_t^\leftarrow |\mathcal{Y}_t^\leftarrow - \mathcal{X}_t^\leftarrow|^2) \int_{\mathbb{R}^d} \varphi^2 \rho_t^\leftarrow + \frac{2\varsigma_t^\leftarrow}{m_t^{\leftarrow 2}} \int_{\mathbb{R}^d} \varphi^2 |\nabla V_t^\leftarrow(x) - \nabla V_t^\leftarrow(\mathcal{Y}_t^\leftarrow)|^2 \rho_t^\leftarrow \\ &= (\xi_t^\leftarrow + 2\varsigma_t^\leftarrow |\mathcal{Y}_t^\leftarrow - \mathcal{X}_t^\leftarrow|^2) \int_{\mathbb{R}^d} \varphi^2 \rho_t^\leftarrow + \frac{2\varsigma_t^\leftarrow}{m_t^{\leftarrow 2}} \int_{\mathbb{R}^d} \varphi^2 |\nabla V_t^\leftarrow(x)|^2 \rho_t^\leftarrow \\ &\stackrel{(34)}{\leq} (\xi_t^\leftarrow + 2\varsigma_t^\leftarrow |\mathcal{Y}_t^\leftarrow - \mathcal{X}_t^\leftarrow|^2) \int_{\mathbb{R}^d} \varphi^2 \rho_t^\leftarrow + \frac{2\varsigma_t^\leftarrow}{m_t^{\leftarrow 2}} (4 \int_{\mathbb{R}^d} |\nabla \varphi|^2 \rho_t^\leftarrow + 2 \int_{\mathbb{R}^d} \varphi^2 \Delta V_t^\leftarrow \rho_t^\leftarrow) \\ &\stackrel{(12)}{\leq} (\xi_t^\leftarrow + 2\varsigma_t^\leftarrow |\mathcal{Y}_t^\leftarrow - \mathcal{X}_t^\leftarrow|^2) \int_{\mathbb{R}^d} \varphi^2 \rho_t^\leftarrow + \frac{2\varsigma_t^\leftarrow}{m_t^{\leftarrow 2}} (4 \int_{\mathbb{R}^d} |\nabla \varphi|^2 \rho_t^\leftarrow + 10M_t^\leftarrow d \int_{\mathbb{R}^d} \varphi^2 \rho_t^\leftarrow) \\ &= (\xi_t^\leftarrow + 2\varsigma_t^\leftarrow |\mathcal{Y}_t^\leftarrow - \mathcal{X}_t^\leftarrow|^2 + \frac{20M_t^\leftarrow d \varsigma_t^\leftarrow}{m_t^{\leftarrow 2}}) \int_{\mathbb{R}^d} \varphi^2 \rho_t^\leftarrow + \frac{8\varsigma_t^\leftarrow}{m_t^{\leftarrow 2}} \int_{\mathbb{R}^d} |\nabla \varphi|^2 \rho_t^\leftarrow. \end{aligned}$$

To get the fifth line, we used the definition of \mathcal{Y}_t^\leftarrow : \mathcal{Y}_t^\leftarrow is the global minimum of V_t^\leftarrow so that $\nabla V_t^\leftarrow(\mathcal{Y}_t^\leftarrow) \equiv 0$. To get the second last line, we used the fact that

$$\Delta V_t^\leftarrow = (1 + \hbar^{-2}) \Delta U_t^\leftarrow - \hbar^{-2} \leq (1 + \hbar^{-2}) dM_t^\leftarrow - \hbar^{-2} \stackrel{\text{(by } \hbar \geq 1/2\text{)}}{\leq} 5dM_t^\leftarrow.$$

□

Proof of Lem. E.3. Note that ς_t^\leftarrow does not depend on \hbar . When $\hbar \rightarrow \infty$, as $V_t^\leftarrow \rightarrow U_t^\leftarrow$ (9), we know $Z_{V_t^\leftarrow}$ converges to $Z_{U_t^\leftarrow} \equiv 1$ by the definition of $p_t := e^{-U_t}$, we immediately know that

$$\lim_{\hbar \rightarrow \infty} |\partial_t \log Z_{V_t^\leftarrow}| = 0.$$

Then

$$\lim_{\mathbf{h} \rightarrow \infty} \xi_t^{\leftarrow} = \frac{5d(1 + M_t^{\leftarrow})}{2} + \frac{5}{2} |\mathcal{X}_t^{\leftarrow}|^2.$$

Moreover, $\mathcal{Y}_t \rightarrow \mathcal{X}_t$ as $\mathbf{h} \rightarrow \infty$, we have

$$\begin{aligned} \lim_{\mathbf{h} \rightarrow \infty} C_t^{\leftarrow, (1)} &= \lim_{\mathbf{h} \rightarrow \infty} \xi_t^{\leftarrow} + 2 \lim_{\mathbf{h} \rightarrow \infty} \varsigma_t^{\leftarrow} |\mathcal{Y}_t^{\leftarrow} - \mathcal{X}_t^{\leftarrow}|^2 + \frac{20dM_t^{\leftarrow}\varsigma_t^{\leftarrow}}{m_t^{\leftarrow 2}}, \\ &= \frac{5d(1 + M_t^{\leftarrow})}{2} + \frac{5}{2} |\mathcal{X}_t^{\leftarrow}|^2 + \frac{(50 + 75M_t^{\leftarrow 2})dM_t^{\leftarrow}}{m_t^{\leftarrow 2}}. \end{aligned}$$

□

APPENDIX F. PROOF OF PROP. 3.5

Case I: $\mathbf{h} = 0$. For this ODE case, (6) becomes

$$(35) \quad \mathcal{L}_t^{(0)}(\mu)(x) = \frac{1}{2} \nabla \cdot \left(\nabla (U_t^{\leftarrow}(x) - |x|^2/2) \mu(x) \right),$$

and the formula of leading order term $L(0)$ is

$$L(0) = \frac{1}{2} \int_{\mathbb{R}^d} \frac{v_T^2(x)}{p_0(x)} dx, \quad v_T \stackrel{(8)}{=} -\frac{1}{2} \int_{T-a}^T \Phi_{t,T}^{(0)}(\nabla \cdot (p_t^{\leftarrow} E)) dt,$$

since we perturb the $\mathcal{E}_t^{\leftarrow}$ only when $t \approx T$, that is, $\mathcal{E}_t^{\leftarrow}(x) = \mathbb{I}_{t \in [T-a, T]} E(x)$ for a small positive a . Then we know that

$$v_T \sim -\frac{1}{2} \int_{T-a}^T \nabla \cdot (p_0 E) dt = -\frac{a}{2} \nabla \cdot (p_0 E).$$

Recall that $p_0 = p_T^{\leftarrow} \approx p_t^{\leftarrow}$ when $t \approx T$; moreover, $\Phi_{t,T}^{(0)} \approx \Phi_{T,T}^{(0)} \equiv \text{Id}$. Therefore, the leading order term of $L(0)$ when $a \ll 1$ is

$$L(0) \sim \frac{a^2}{8} \int_{\mathbb{R}^d} \frac{(\nabla \cdot (p_0 E))^2}{p_0}.$$

Case II: $\mathbf{h} \rightarrow \infty$. For the SDE case,

$$\begin{aligned} v_T &\stackrel{(8)}{=} -\frac{1 + \mathbf{h}^2}{2} \int_0^T \Phi_{t,T}^{(\mathbf{h})}(\nabla \cdot (p_t^{\leftarrow} \mathcal{E}_t^{\leftarrow})) dt \\ &\sim -\frac{1 + \mathbf{h}^2}{2} \int_{T-a}^T \Phi_{t,T}^{(\mathbf{h})}(\nabla \cdot (p_0 E)) dt \quad (\text{by } a \ll 1) \\ &\sim -\frac{1 + \mathbf{h}^2}{2} \int_{T-a}^T e^{(T-t)\frac{\mathbf{h}^2}{2} \mathcal{K}_T^{\leftarrow}} (\nabla \cdot (p_0 E)) dt \quad (\text{by } a \ll 1) \\ &= -\frac{1 + \mathbf{h}^2}{2} \int_0^a e^{t\frac{\mathbf{h}^2}{2} \mathcal{K}_T^{\leftarrow}} (\nabla \cdot (p_0 E)) dt, \end{aligned}$$

where

$$(36) \quad \mathcal{K}_t^{\leftarrow}(\mu) := \Delta \mu + \nabla \cdot (\nabla V_t^{\leftarrow} \mu).$$

Then when we further assume $\hbar \gg 1$,

$$\begin{aligned}
\frac{1}{2} \int_{\mathbb{R}^d} \frac{(v_T)^2}{p_0} &\lesssim \frac{1}{2} \int_{\mathbb{R}^d} \frac{(v_T)^2}{\rho_0} && \text{(by Lem. E.1 iii)} \\
&\lesssim \frac{(1 + \hbar^2)^2}{8} \left(\frac{1 - e^{-a \frac{\hbar^2}{2} \kappa_0}}{\frac{\hbar^2}{2} \kappa_0} \right)^2 \int_{\mathbb{R}^d} \frac{(\nabla \cdot (p_0 E))^2}{\rho_0} && \text{(by Lem. D.2)} \\
&\sim \frac{(1 + \hbar^2)^2}{\hbar^4} \frac{(1 - e^{-a \frac{\hbar^2}{2} \kappa_0})^2}{2\kappa_0^2} \int_{\mathbb{R}^d} \frac{(\nabla \cdot (p_0 E))^2}{\rho_0} \\
&\sim \frac{(1 - e^{-a \frac{\hbar^2}{2} \kappa_0})^2}{2\kappa_0^2} \int_{\mathbb{R}^d} \frac{(\nabla \cdot (p_0 E))^2}{\rho_0} \\
&\sim \frac{(1 - e^{-a \frac{\hbar^2}{2} \kappa_0})^2}{2\kappa_0^2} \int_{\mathbb{R}^d} \frac{(\nabla \cdot (p_0 E))^2}{p_0}.
\end{aligned}$$

To apply Lem. D.2 in the second line, we remark that $\mathcal{K}_T^\leftarrow(\mu) = \Delta\mu + \nabla \cdot (\nabla V_T^\leftarrow \mu)$, V_T^\leftarrow has Hessian lower bound $\kappa_T^\leftarrow \equiv \kappa_0$ (14).

APPENDIX G. PROOF OF PROP. 3.6

Let us pick an $a = \hbar^{-\beta} \ll 1$. We split v_T (8) into two parts:

$$\begin{aligned}
v_T &= -\frac{1 + \hbar^2}{2} \int_0^T \Phi_{t,T}^{(h^\leftarrow)} \left(\underbrace{\nabla \cdot (p_t^\leftarrow \mathcal{E}_t^\leftarrow)}_{=: \Gamma_t^\leftarrow} \right) dt \\
&= -\frac{1 + \hbar^2}{2} \int_{T-a}^T \Phi_{t,T}^{(h^\leftarrow)} (\Gamma_t^\leftarrow) dt - \frac{1 + \hbar^2}{2} \int_0^{T-a} \Phi_{t,T}^{(h^\leftarrow)} (\Gamma_t^\leftarrow) dt.
\end{aligned}$$

Upper bound. By Cauchy-Schwartz inequality ($(x+y)^2 = x^2 + y^2 + 2xy \leq (1 + \alpha^2)x^2 + (1 + \alpha^{-2})y^2$ for any x, y and $\alpha > 0$),

$$\begin{aligned}
L(\hbar) &= \frac{1}{2} \int \frac{v_T^2}{p_0} \\
&\leq (1 + \alpha^2) \underbrace{\frac{(1 + \hbar^2)^2}{8} \int_{\mathbb{R}^d} \frac{\left(\int_{T-a}^T \Phi_{t,T}^{(h^\leftarrow)} (\Gamma_t^\leftarrow) dt \right)^2}{p_0}}_{=: \mathcal{T}_1} \\
&\quad + (1 + \alpha^{-2}) \underbrace{\frac{(1 + \hbar^2)^2}{8} \int_{\mathbb{R}^d} \frac{\left(\int_0^{T-a} \Phi_{t,T}^{(h^\leftarrow)} (\Gamma_t^\leftarrow) dt \right)^2}{p_0}}_{=: \mathcal{T}_2}.
\end{aligned}$$

For the second term \mathcal{T}_2 ,

$$\begin{aligned}
\mathcal{T}_2 &= \frac{(1+h^2)^2}{8} \int_{\mathbb{R}^d} \frac{\left(\int_0^{T-a} \Phi_{t,T}^{(h^\leftarrow)}(\Gamma_t^\leftarrow) dt\right)^2}{p_0} \\
&\stackrel{\text{Cauchy ineq.}}{\leq} \frac{(1+h^2)^2(T-a)}{8} \int_0^{T-a} \left(\int_{\mathbb{R}^d} \frac{\Phi_{t,T}^{(h^\leftarrow)}(\Gamma_t^\leftarrow)^2}{p_0} dt\right) \\
&\stackrel{(25)}{\leq} \frac{(1+h^2)^2 T}{2} \int_0^{T-a} \left(\int_{\mathbb{R}^d} \frac{\Phi_{t,T}^{(h^\leftarrow)}(\Gamma_t^\leftarrow)^2}{\rho_0} dt\right) \\
&\stackrel{(29)}{\leq} \frac{(1+h^2)^2 T}{2} \int_0^{T-a} \left(\int_{\mathbb{R}^d} \frac{\Gamma_t^{\leftarrow 2}}{\rho_t^\leftarrow} dt\right) \exp\left(-\int_t^T ((h^2 - C_r^{\leftarrow, (2)}) \kappa_r^\leftarrow - C_r^{\leftarrow, (1)}) dr\right) dt \\
&\leq \frac{(1+h^2)^2 T}{2} \sup_{t \in [0, T]} \left(\int_{\mathbb{R}^d} \frac{\Gamma_t^{\leftarrow 2}}{\rho_t^\leftarrow} dt\right) \exp\left(\int_0^T C_r^{\leftarrow, (2)} \kappa_r^\leftarrow + C_r^{\leftarrow, (1)} dr\right) \int_0^{T-a} e^{-h^2 \gamma(T-t)} dt \\
&\leq \frac{(1+h^2)T}{2h^2} \sup_{t \in [0, T]} \left(\int_{\mathbb{R}^d} \frac{\Gamma_t^{\leftarrow 2}}{\rho_t^\leftarrow} dt\right) \exp\left(\int_0^T C_r^{\leftarrow, (2)} \kappa_r^\leftarrow + C_r^{\leftarrow, (1)} dr\right) \frac{(1+h^2)e^{-ah^2\gamma}}{\gamma},
\end{aligned}$$

which decays exponentially fast as $h \rightarrow \infty$ as long as $h^2 \gg a^{-1} \gg 1$. To get the second line above, we used Cauchy-Schwarz inequality and Fubini's theorem. Recall the definition of $\gamma \in \mathbb{R}^+$ in the statement of Prop. 3.6.

Overall, when $a = h^{-\beta} \ll 1$,

$$L(h) \leq (1+\alpha^{-2}) C \frac{(1+h^2) \exp(-h^{2-\beta}\gamma)}{\gamma} + (1+\alpha^2)\mathcal{T}_1,$$

where

$$C = \frac{(1+h^2)T}{2h^2} \sup_{t \in [0, T]} \left(\int_{\mathbb{R}^d} \frac{\Gamma_t^{\leftarrow 2}}{\rho_t^\leftarrow} dt\right) \exp\left(\int_0^T C_r^{\leftarrow, (2)} \kappa_r^\leftarrow + C_r^{\leftarrow, (1)} dr\right).$$

Lower bound. The lower bound can be proved in the same way: by Cauchy-Schwarz inequality again,

$$\begin{aligned}
L(h) &\geq (1-\alpha^2)\mathcal{T}_1 + (1-\alpha^{-2})\mathcal{T}_2 \\
&\geq (1-\alpha^2)\mathcal{T}_1 - (\alpha^{-2}-1)C \frac{(1+h^2) \exp(-h^{2-\beta}\gamma)}{\gamma}.
\end{aligned}$$

The remaining task is to estimate \mathcal{T}_1 .

Asymptotic limit of \mathcal{T}_1 . We only provide an asymptotic result below. As $a \ll 1$,

$$\begin{aligned}
\mathcal{T}_1 &:= \frac{(1+h^2)^2}{8} \int_{\mathbb{R}^d} \frac{\left(\int_{T-a}^T \Phi_{t,T}^{(h^\leftarrow)}(\Gamma_t^\leftarrow) dt\right)^2}{p_0} \\
&\sim \frac{(1+h^2)^2}{8} \int_{\mathbb{R}^d} \frac{1}{p_0} \left(\left(\int_{T-a}^T \Phi_{t,T}^{(h^\leftarrow)} dt\right) (\Gamma_T^\leftarrow)\right)^2 \\
&\sim \frac{(1+h^2)^2}{8} \int_{\mathbb{R}^d} \frac{1}{p_0} \left(\int_{T-a}^T \exp\left(\frac{h^2}{2}(T-t)\mathcal{K}_T^\leftarrow\right) \Gamma_T^\leftarrow dt\right)^2 \\
&\sim \frac{(1+h^2)^2}{8} \int_{\mathbb{R}^d} \frac{1}{\rho_0} \left(\int_{T-a}^T \exp\left(\frac{h^2}{2}(T-t)\mathcal{K}_T^\leftarrow\right) \Gamma_T^\leftarrow dt\right)^2,
\end{aligned}$$

where we used $\Gamma_t^\leftarrow \approx \Gamma_T^\leftarrow$, when $t \approx T$ in the second line; we used $\frac{\mathcal{L}_t^{(h^\leftarrow)}}{h^2/2} \approx \frac{\mathcal{L}_T^{(h^\leftarrow)}}{h^2/2}$ when $t \approx T$ in the third line; $\mathcal{L}_T^{(h^\leftarrow)} = h^2/2 \mathcal{K}_T^\leftarrow$ (36) herein. In the last line, we used the fact that $\rho_0 \sim p_0$ when $h \rightarrow \infty$.

By Lem. D.2, we know that

$$\begin{aligned} \mathcal{T}_1 &\sim \frac{(1+h^2)^2}{8} \sum_{k=1}^{\infty} \left(\frac{1-e^{-a\frac{h^2}{2}\lambda_k^{(h)}}}{\frac{h^2}{2}\lambda_k^{(h)}} \right)^2 (\alpha_k^{(h)})^2 \\ &\sim \frac{1}{2} \sum_{k=1}^{\infty} \left(\frac{\alpha_k^{(h)}}{\lambda_k^{(h)}} \right)^2 \quad (\text{by } a = h^{-\beta}, h \gg 1), \end{aligned}$$

where $(\lambda_k^{(h)}, \phi_k^{(h)})$ are eigen pairs of \mathcal{K}_T^\leftarrow and $\Gamma_T^\leftarrow = \sum_{k=1}^{\infty} \alpha_k^{(h)} \phi_k^{(h)}$. When $h \rightarrow \infty$, we know that the eigenvalues of \mathcal{K}_T^\leftarrow , which depends on h and has the form

$$\mathcal{K}_T^\leftarrow(\mu)(x) = \Delta\mu(x) + \nabla \cdot (\nabla U_0(x)\mu(x)) + h^{-2} \nabla \cdot ((\nabla U_0(x) - x)\mu)$$

should converge to \mathcal{K}^∞ , defined as

$$\mathcal{K}^\infty(\mu) := \Delta\mu + \nabla \cdot (\nabla U_0\mu).$$

Therefore, in the limit,

$$\lim_{h \rightarrow \infty} \mathcal{T}_1 = \frac{1}{2} \sum_{k=1}^{\infty} \left(\alpha_k^{(\infty)} / \lambda_k^{(\infty)} \right)^2,$$

where $(\lambda_k^{(\infty)}, \phi_k^{(\infty)})$ are eigen pairs of \mathcal{K}^∞ and $\Gamma_T^\leftarrow = \sum_{k=1}^{\infty} \alpha_k^{(\infty)} \phi_k^{(\infty)}$.

Upper bound of \mathcal{T}_1 . By the upper bound in Lem. D.2 (together with $a = h^{-\beta}$ and $h \gg 1$) or by applying $\lambda_k^{(h)} \geq \kappa_0$ directly to the asymptotic of \mathcal{T}_1 , when $h \gg 1$,

$$\begin{aligned} \mathcal{T}_1 &\lesssim \frac{1}{2\kappa_0^2} \int_{\mathbb{R}^d} \frac{\Gamma_T^\leftarrow}{\rho_0} \\ &= \frac{1}{2\kappa_0^2} \int_{\mathbb{R}^d} \frac{(\nabla \cdot (p_T^\leftarrow \mathcal{E}_T^\leftarrow))^2}{\rho_0} \\ &\sim \frac{1}{2m_0^2} \int_{\mathbb{R}^d} \frac{(\nabla \cdot (p_0 \mathcal{E}_T^\leftarrow))^2}{p_0}. \end{aligned}$$

The term \mathcal{T} in Prop. 3.6 is simply the limit of \mathcal{T}_1 .

APPENDIX H. NUMERICAL EXPERIMENT: 1D GAUSSIAN CASE

We want to demonstrate and validate main findings via a simple 1D Gaussian. Suppose $f_t(x) = -\frac{1}{2}x$, $g_t = 1$, and the exact data distribution is a Gaussian $p_0 = \mathcal{N}(0, \sigma_0^2)$. The error is quantified by $\text{KL}(p_0 || \tilde{q}_T)$. We investigate this error as a function of the magnitude of h^\leftarrow (which is chosen as a constant function $h_t^\leftarrow = h$ for any $t \in [0, T]$).

H.1. Explicit formulas for 1D Gaussian case. From solving the SDE for the forward process, we know that

$$(37) \quad p_t = \mathcal{N}(0, \sigma_t^2), \quad \sigma_t^2 = \sigma_0^2 e^{-t} + 1 - e^{-t}, \quad \nabla \log p_t(x) = -\frac{x}{\sigma_t^2}.$$

The backward dynamics (5) on $t \in [0, T]$ is

$$\begin{cases} d\tilde{Y}_t = \left(\frac{1}{2}\tilde{Y}_t + \frac{1+h_t^{\leftarrow 2}}{2} \left(-\frac{\tilde{Y}_t}{\sigma_{T-t}^2} + \epsilon \mathcal{E}_t^{\leftarrow}(\tilde{Y}_t) \right) \right) dt + h_t^{\leftarrow} dW_t, \\ \text{law}(\tilde{Y}_0) = p_T. \end{cases}$$

In this example, there is only one source of error, which is $\mathcal{E}_t^{\leftarrow}$, as we know explicitly the distribution p_T and we can choose the time step small enough such that numerical discretization error is negligible. Due to the structure of the score function, it is reasonable to consider the following ansatz

$$(38) \quad \mathcal{E}_t^{\leftarrow}(x) = \alpha_t x.$$

This example has explicit formulas: \tilde{Y}_T is a Gaussian distribution with $\mathbb{E}[\tilde{Y}_T] = 0$ and

$$\text{Var}(\tilde{Y}_T) = G_T^{-2} \text{Var}(\tilde{Y}_0) + \int_0^T G_T^{-2} G_t^2 h_t^{\leftarrow 2} dt,$$

where

$$G_t := \exp \left(- \int_0^t \frac{1}{2} + \frac{1+h_s^{\leftarrow 2}}{2} \left(-\frac{1}{\sigma_{T-s}^2} + \epsilon \alpha_s \right) ds \right).$$

The error under consideration also has an explicit formula:

$$\text{KL}(p_0 || \tilde{q}_T) = \frac{1}{2} \log \left(\frac{\text{Var}(\tilde{Y}_T)}{\sigma_0^2} \right) + \frac{\sigma_0^2}{2 \text{Var}(\tilde{Y}_T)} - \frac{1}{2}.$$

H.2. Experiment 1: Fixed error magnitude ϵ and we consider various error types. We choose $T = 2$, $h_t^{\leftarrow} = h$ for all $t \in [0, T]$, and the error function is chosen as

$$(39) \quad \epsilon = 0.02, \quad \mathcal{E}_t^{\leftarrow}(x) = \nabla \log p_t^{\leftarrow}(x) \times \begin{cases} 1 & \text{case 1;} \\ -1 & \text{case 2;} \\ \frac{1 + \sin(2\pi t/T)}{2} & \text{case 3;} \\ \mathbb{I}_{t < 0.95T} & \text{case 4} \\ \mathbb{I}_{t > 0.99T} & \text{case 5.} \end{cases}$$

For these choices, we only perturb the true score function by a bounded prefactor. We can observe that the error $\text{KL}(p_0 || \tilde{q}_T)$ is a complicated function of h in general; see Fig. 6. When we only perturb the score function during initial period of the generative process (case 4), we can clearly observe that error decays exponentially fast with respect to h^2 , which is compatible with Prop. 3.4. When we only perturb the score function near the end of the generative process (case 5), increasing the diffusion coefficient will actually increase the error, which is predicted by Prop. 3.5. For a general error (case 1, 2, 3), overall we can still expect that increasing diffusion coefficient h will generally suppress the error when σ_0 is small.

H.3. Experiment 2: We consider $L(h)$ for various error types. We further consider approximating $L(h) \equiv L(h, \mathcal{E}^\leftarrow, p_0)$ from linear regression and study how σ_0 (namely the data distribution p_0), error type \mathcal{E}^\leftarrow , and h affect the leading order term $L(h, \mathcal{E}^\leftarrow, p_0)$. Recall that we use $L(h)$ as a short-hand notation when \mathcal{E}^\leftarrow and p_0 are clear from context; see § 3. As a remark, to approximate $L(h)$, we used the leading-order approximation that $\text{KL}(p_0 || \tilde{q}_T) = L(h)\epsilon^2 + \mathcal{O}(\epsilon^3)$: we choose a few ϵ values and use linear regression to estimate $L(h)$.

In Fig. 7, we can more clearly observe that $L(h)$ converges to a constant extremely fast when h increases for cases $\sigma_0 < 1$. The value of \mathcal{E}_T^\leftarrow for the case 3 is only 1/2 of that for case 1 and case 2. By Prop. 3.6, we know that $\lim_{h \rightarrow \infty} L(h)$ for the case 3 should be approximated 1/4 of that for cases 1 and 2. This is also numerically observed in Table 2.

TABLE 2. Approximated value of $L(h)$ when $h^2 \approx 20$. We can observe that within each column (referring to a specific error type) the value is almost independent of the σ_0 in particular when σ_0 is relatively small ($\sigma_0 < 1$).

σ_0	Case 1	Case 2	Case 3
0.2	0.2567	0.3032	0.0658
0.4	0.2569	0.3028	0.0636
0.6	0.2570	0.3018	0.0597
0.8	0.2569	0.3023	0.0544
1.5	0.2570	0.3017	0.0321
2.0	0.2564	0.3022	0.0198
3.0	0.2566	0.3020	0.0121

APPENDIX I. MORE DETAILS ABOUT NUMERICAL EXPERIMENTS IN § 4

In this section, we discuss datasets, network architectures, evaluation metrics, weights in denoising score matching, and numerical schemes (exponential integrator). More technical details can be found in our source code available at <https://anonymous.4open.science/r/OptimalDiffusion-FE0C/>.

I.1. Datasets.

- **1D 2-mode Gaussian mixture:** $p_0(x) = \sum_{i=1}^2 0.5\mathcal{N}(x; (-1.0)^i, 0.01)$.
- **2D 4-mode Gaussian mixture:** $p_0(x) = \sum_{i,j=1}^2 0.25\mathcal{N}(x; ((-1.0)^i, (-1.0)^j), 0.05^2 \mathbf{I}_2)$.
- **Swiss roll:** Swiss roll generates samples by $(x, y) = (t \sin(t), t \cos(t))$ with t drawn from uniform distribution $\mathcal{U}(\frac{3\pi}{2}, \frac{9\pi}{2})$.
- **MNIST:** MNIST [29] contains 60,000 28×28 gray-scale images with hand-written digits.

I.2. Network architectures and other parameters. For experiments on 1D/2D Gaussian mixtures, the exact scores can be obtained analytically when using VP-SDE. We set $T = 4$ and $g(t) = 1$ for $t \in [0, T]$. For the time discretization when solving the reverse SDE with Euler-Maruyama method, we apply 40,000 steps and 80,000 steps for 1D and 2D Gaussian mixtures, respectively.

For experiments on Swiss roll, we apply a three-layer neural network for score matching, where the width of each layer is set as 50, 50, and 2 and we apply ReLU as the nonlinear activation for two hidden layers. We set $T = 1$ and $g(t) = \sqrt{0.1(1-t) + 20t}$ for $t \in [0, T]$. The learning rate is set as 0.01 and decays by 0.5 every 8,000 steps. The batch size is set as 400. We train the neural network for 20,000 steps. For the time discretization when solving the reverse SDE with Euler-Maruyama method, we apply 20,000 steps.

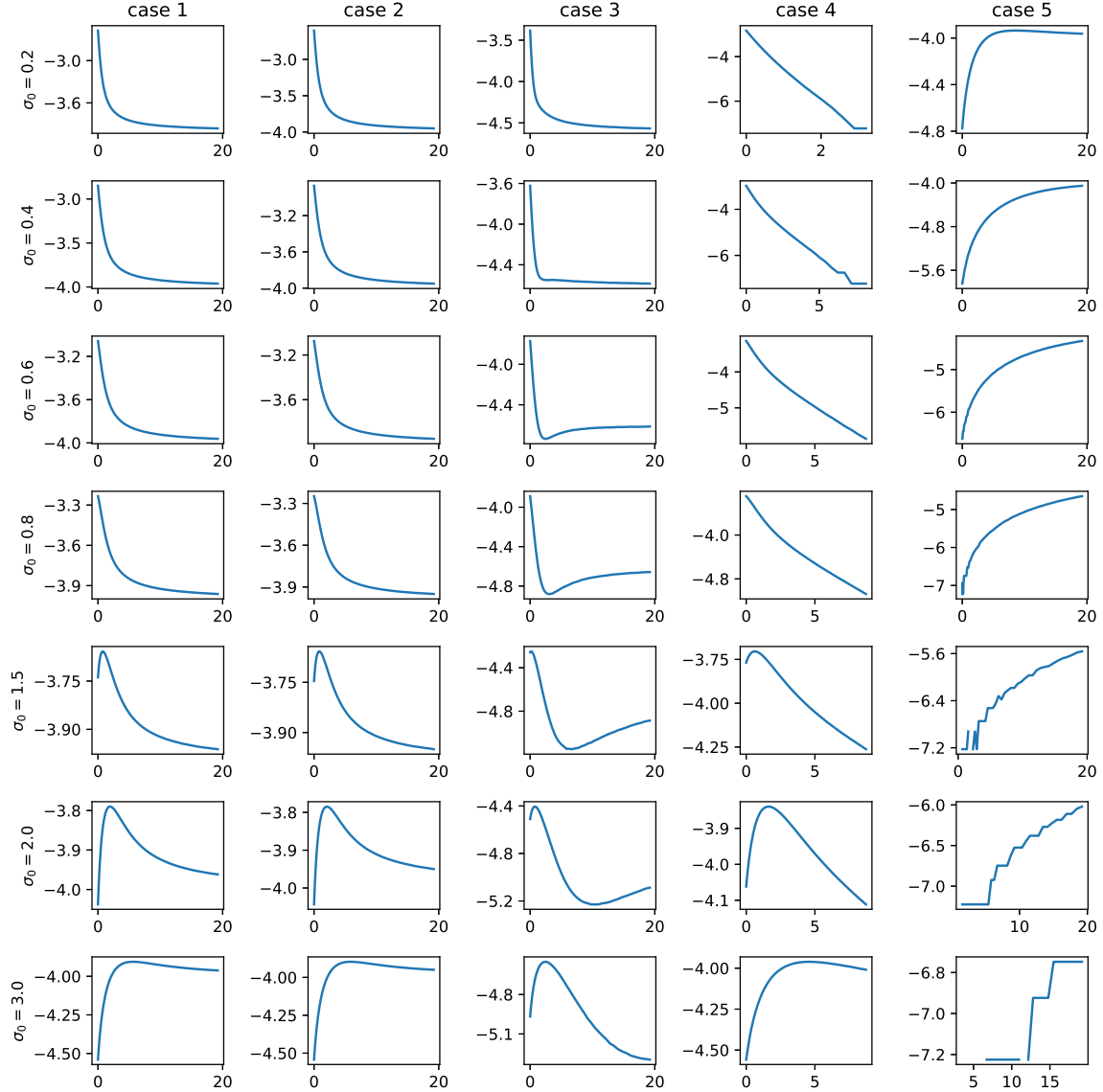


FIGURE 6. We show $\log_{10}(\text{KL}(p_0||q_T))$ as a function of h^2 for the 1D Gaussian model. $T = 2$, different σ_0 and error functions in (39) are considered.

For experiments on MNIST, we apply the net architecture in [16] for score matching, where we use two resolution blocks in U-net and set the multipliers of channels to be one and two. We set $T = 1.4$ and $g(t) = \sqrt{0.1(1-t) + 20t}$ for $t \in [0, T]$. The number of iteration is 20,000, the batch size is set as 64. We solve the reverse SDE with exponential integrator; see the formula in the later part of this Appendix.

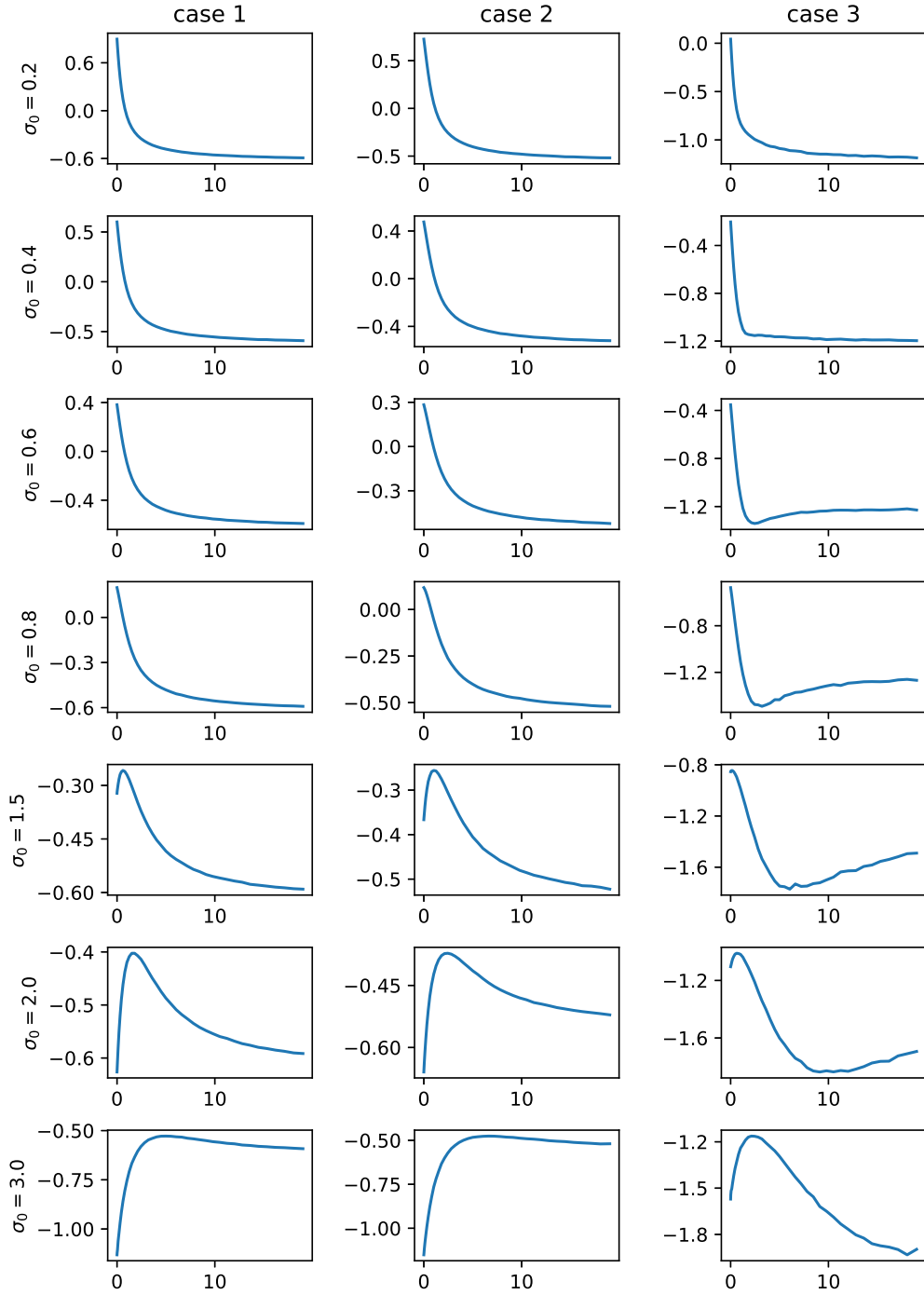


FIGURE 7. We show $L(h)$ as a function of h^2 for the 1D Gaussian model. $T = 2$, different σ_0 and error functions in (39) are considered.

I.3. Evaluation metrics. For experiments of 1D/2D Gaussian mixtures and Swiss roll, we apply approximated divergences for evaluating the performances. Specifically, we discretize the space into 100 bins in each dimension, then obtain the empirical densities of 10,000 true samples and 10,000 generated samples, and use Jensen-Shannon divergence, Kullback-Leibler divergence and Wasserstein distance between both empirical densities as the metrics for evaluation.

I.4. Training the score function: Denoising score matching. Denoising score matching [28] refers to the following loss function to train the score:

$$\min_{\mathfrak{S}} \int_0^T \omega_t \mathbb{E}_{p_0} \mathbb{E}_{p_{t|0}} \left[\left\| \mathfrak{S}_t(X_t) - \nabla \log p_{t|0}(X_t|X_0) \right\|^2 \right] dt,$$

where $p_{t|0}(x_t|x_0)$ is the transition probability of the state x_0 at time 0 towards the state x_t at time t for the forward process (1). Note that, given the fixed X_0 , we can express the solution of (1) (with the choice $f_t(x) = -\frac{g_t^2}{2}x$) at time t as

$$X_t = (G_t)^{-1} X_0 + \int_0^t G_t^{-1} G_s g_s \, dW_s,$$

where $G_t = \exp \left(\int_0^t \frac{g_s^2}{2} \, ds \right)$ herein. The standard deviation of the Brownian motion term above is

$$\varpi_t := \sqrt{\int_0^t G_t^{-2} G_s^2 g_s^2 \, ds}.$$

When $g_t = \sqrt{\beta_0 + (\beta_1 - \beta_0)t}$ as used in many literature [25, 16], we can explicitly solve for ϖ_t :

$$\varpi_t = \sqrt{1 - \exp \left(-\frac{1}{2} t^2 (\beta_1 - \beta_0) - t \beta_0 \right)}.$$

In literature, a common choice of ω is that (see e.g., [16, 25])

$$(40) \quad \omega_t = \varpi_t^2 \quad \text{refereed as the \textbf{default} weight.}$$

We also test two other cases:

$$(41) \quad \omega_t = \begin{cases} \varpi_t^3 & \text{noise-driven, or simply referred as \textbf{“noise”};} \\ \frac{\varpi_t^2}{0.25 + \varpi_t} & \text{data-driven, or simply referred as \textbf{“data”}.} \end{cases}$$

Note that ϖ is an increasing function with range $[0, 1]$ (in particular, $\varpi_0 = 0$ and $\lim_{t \rightarrow \infty} \varpi_t = 1$). Compared to the loss function for the default case, the data-driven case places relatively more weight towards the time region closer to the data distribution p_0 and the noise-driven case places more weight towards the noise region near $\mathcal{N}(0, I_d)$.

I.5. Exponential integrator. We shall explain the exponential integrator for (2) with $t \in [0, T]$, i.e., the following equation

$$\begin{aligned} dY_t &= -f_t^\leftarrow(Y_t) \, dt + \frac{(g_t^\leftarrow)^2 + (h_t^\leftarrow)^2}{2} \nabla \log p_t^\leftarrow(Y_t) \, dt + h_t^\leftarrow \, dW_t \\ &= \frac{1}{2} g_t^{\leftarrow 2} Y_t \, dt + \frac{(g_t^\leftarrow)^2 + (h_t^\leftarrow)^2}{2} \nabla \log p_t^\leftarrow(Y_t) \, dt + h_t^\leftarrow \, dW_t. \end{aligned}$$

Then for any time $t \in [t_k, t_{k+1}]$, and given \hat{Y}_{t_k} , we approximate the above dynamics by

$$d\hat{Y}_t \approx \frac{1}{2} g_t^{\leftarrow 2} \hat{Y}_t dt + \frac{(g_t^{\leftarrow})^2 + (h_t^{\leftarrow})^2}{2} \nabla \log p_{t_k}^{\leftarrow}(\hat{Y}_{t_k}) dt + h_t^{\leftarrow} dW_t.$$

This dynamics is a linear SDE and we can solve it exactly

$$\begin{aligned} \hat{Y}_{t_{k+1}} &= \underbrace{e^{\frac{1}{2} \int_{t_k}^{t_{k+1}} g_s^{\leftarrow 2} ds} \hat{Y}_{t_k} + \left[\int_{t_k}^{t_{k+1}} e^{\frac{1}{2} \int_t^{t_{k+1}} g_s^{\leftarrow 2} ds} \frac{g_t^{\leftarrow 2} + h_t^{\leftarrow 2}}{2} dt \right] \mathbf{S}_k}_{=: \mathcal{T}_1} \\ &\quad + \underbrace{\int_{t_k}^{t_{k+1}} e^{\frac{1}{2} \int_t^{t_{k+1}} g_s^{\leftarrow 2} ds} h_t^{\leftarrow} dt}_{=: \mathcal{T}_2} dW_t, \\ \mathbf{S}_k &:= \nabla \log p_{t_k}^{\leftarrow}(\hat{Y}_{t_k}). \end{aligned}$$

Therefore,

$$\hat{Y}_{t_{k+1}} = \mathcal{T}_1 + \sqrt{\int_{t_k}^{t_{k+1}} (\mathcal{T}_2)^2 dt} Z_k, \quad Z_k \sim \mathcal{N}(0, I_d).$$

Suppose that we pick

$$\begin{cases} h_t^{\leftarrow} = \alpha g_t^{\leftarrow}, & \alpha \in \mathbb{R}^+, \\ g_t = \sqrt{\beta_0 + (\beta_1 - \beta_0)t} \end{cases} \quad \text{which implies that} \quad g_t^{\leftarrow} = \sqrt{\beta_0 + (\beta_1 - \beta_0)(T - t)}.$$

Then by straightforward calculations,

$$\hat{Y}_{t_{k+1}} = \gamma_k \hat{Y}_{t_k} + (1 + \alpha^2) (\gamma_k - 1) \mathbf{S}_k + \sqrt{\alpha^2 (\gamma_k^2 - 1)} Z_k,$$

where $\delta_k := t_{k+1} - t_k$ and $\gamma_k := \exp\left(\frac{\delta_k (2\beta_0 + (2t_k - 2T + \delta_k)(\beta_0 - \beta_1))}{4}\right)$.

APPENDIX J. MORE NUMERICAL RESULTS FOR EXPERIMENTS IN § 4

We present more numerical results on 1D Gaussian mixture, Swiss roll, and MNIST to further verify theoretical results.

1D Gaussian mixture. We evaluate the performances of generative models under different values of h for 1D Gaussian mixture, and present the visualization and numerical results in Fig. 8 and Fig. 9, respectively. In Fig. 8, a clear trend shows that with increasing h , the empirical density of generated samples better matches the true density function. This trend is more quantitatively captured in Fig. 9, from which we clearly observe that the distance between the empirical and the true density function decreases to the numerical threshold exponentially fast. Numerical threshold means the error of various distances when $\epsilon = 0$; due to the space discretization when computing various distances, the numerical values of various distances are not exactly zero even when we use the exact score function. However, increasing h can help us to almost reach this limit and this phenomenon is theoretically described in Prop. 3.4.

Swiss roll. In Fig. 10, we provide additional figures to discuss the effect of time-discretization. When the numerical error is negligible, we can observe that the generative process with a larger h can provide a clearer picture of Swiss roll, as shown in Fig. 10c. However, when the discretization error cannot be ignored, the conclusion may be reversed. Therefore, it is necessary to design and employ more accurate numerical methods for models with large h in order to fully benefit from diffusion models with a large diffusion coefficient.

In Fig. 11, we display JS and KL divergences between the true density p_0 and the generated samples. Since the data distribution of Swiss roll is highly localized (data is concentrated on a curve embed in 2D), accurately computing the KL divergence poses a significant numerical challenge. That is why we use Wasserstein distance instead in Fig. 4a. Based on more robust symmetric metrics (i.e., the JS and Wasserstein distance herein), we can observe that a larger h can indeed diminish the error in sample generation.

MNIST. We conduct further experiments to explore the effect of h , the weight function in score-training, as well as the time discretization steps. It is important to note that if one has an extremely well trained score function, then the effect of h is indeed negligible, as shown in (3). To somewhat magnify the score training error for MNIST (but with a reasonable score function), we increase the time T and more importantly, use a **smaller architecture with fewer parameters**; the reason of the occasional failure to generate clear MNIST images in later figures comes from the deliberate experimental design of using a **small architecture**.

We summarize findings as follows:

- For an existing pre-trained score function with non-negligible error, we notice that increasing h can almost ubiquitously improve the quality of sample generation; see Fig. 13 ~ Fig. 18. This improvement is supported by our theoretical results, particularly Prop. 3.4. Notably, even when choosing $h = 0$ (ODE) and $h = g$ (the default diffusion model in many studies) occasionally fail to generate an image, simply by increasing h (possibly with more computational costs), we have a larger chance of generating an image with reasonable quality; for instance, see the last row in Fig. 13. In particular, the ODE-based model sometimes fails to generate hand-writing digits even when the step number is 1000, whereas the diffusion model (with large h) does **not** encounter this issue.

The conclusion might be reversed when the time step size is large, which is similarly observed in the Swiss roll.

- If we are willing to train or re-train the score function and are interested in using the ODE-based model (for fast sample generation), it appears that choosing a noise-driven weight is more suitable for the probability flow than the default choice in literature. Refer to Fig. 5 and Fig. 12 for independent trials using different random seed. This phenomenon aligns with the insight that ODE-based generative models are more affected by the score training error in the initial stage of the generative process (at least compared to the diffusion model with non-vanishing diffusion coefficients).

The computational cost of SDE-based models with large diffusion ($h > g$) is relatively high due to the necessity of a larger number of time steps. However, this can be offset by the ability to use a lightweight architecture that speeds up the generative process. A detailed comparison of various diffusion-based models with the same computational budget constraint is challenging and is slightly beyond the scope of this work, and we will leave this task to future work.

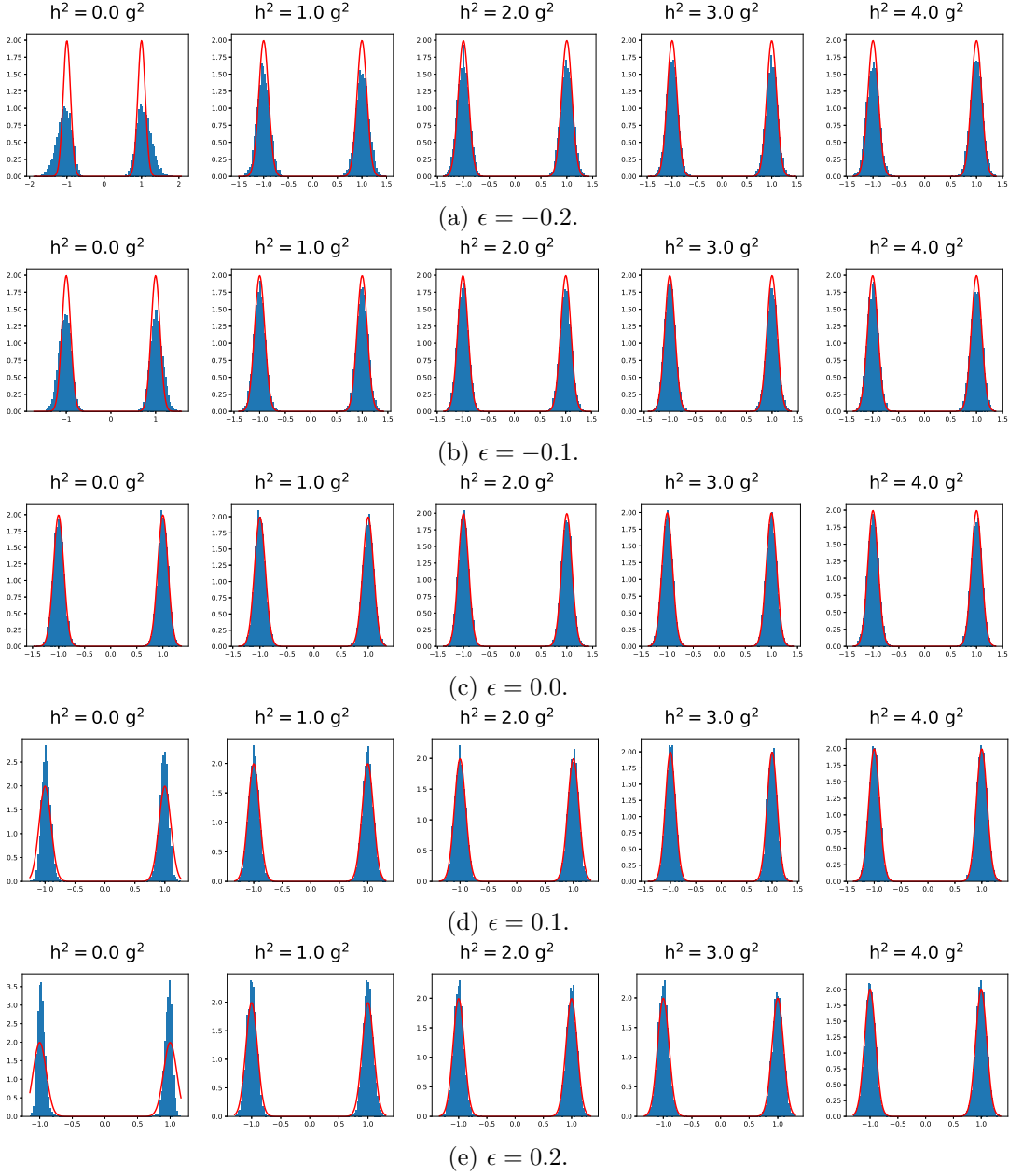


FIGURE 8. Visualization of 1D GMM, where $\mathcal{E}_t^{\leftarrow}(x) = \nabla \log p_t^{\leftarrow}(x)$. We can observe that increasing h can help to generate samples with a distribution closer to the true p_0 .

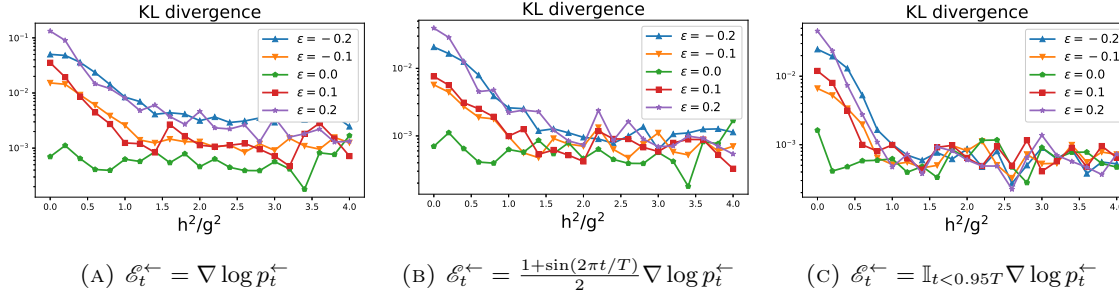


FIGURE 9. Numerical results of 1D 2-mode Gaussian mixture. We can observe that the distance between the empirical density and the true density function decreases as h increases, when \mathcal{E}_T^- is not extremely large.

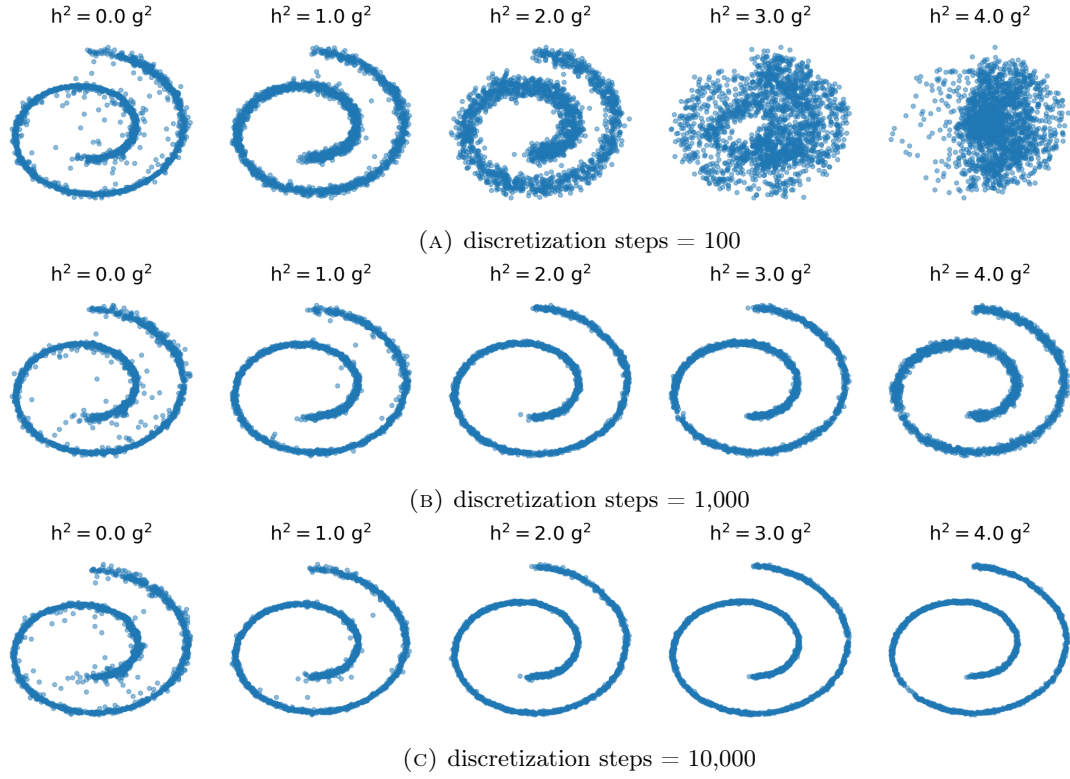


FIGURE 10. Visualization results of Swiss roll with different number of time steps.

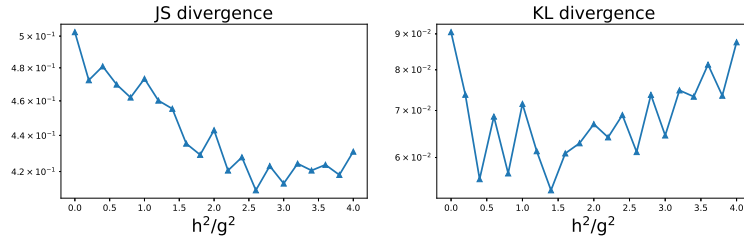


FIGURE 11. Numerical results of Jensen-Shannon divergence and Kullback-Leibler divergence of Swiss roll.



FIGURE 12. $h^2/g^2 = 0$, number of time steps is 1000, trial number 2.

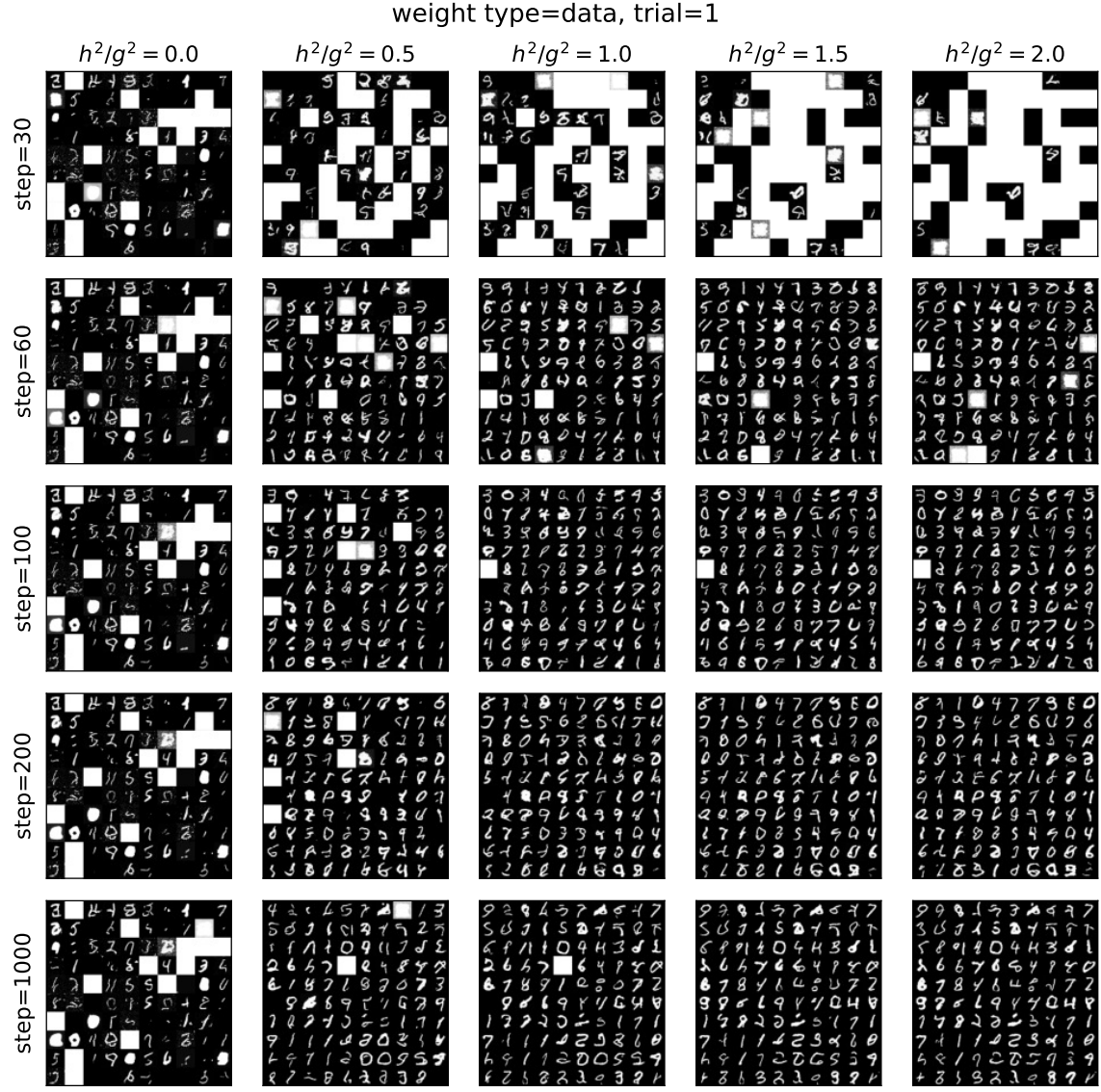


FIGURE 13. Visualization of sample generation in MNIST where we used **data-driven weight** ω (41). We use different random seed to ensure robustness and this is the result for trial 1.

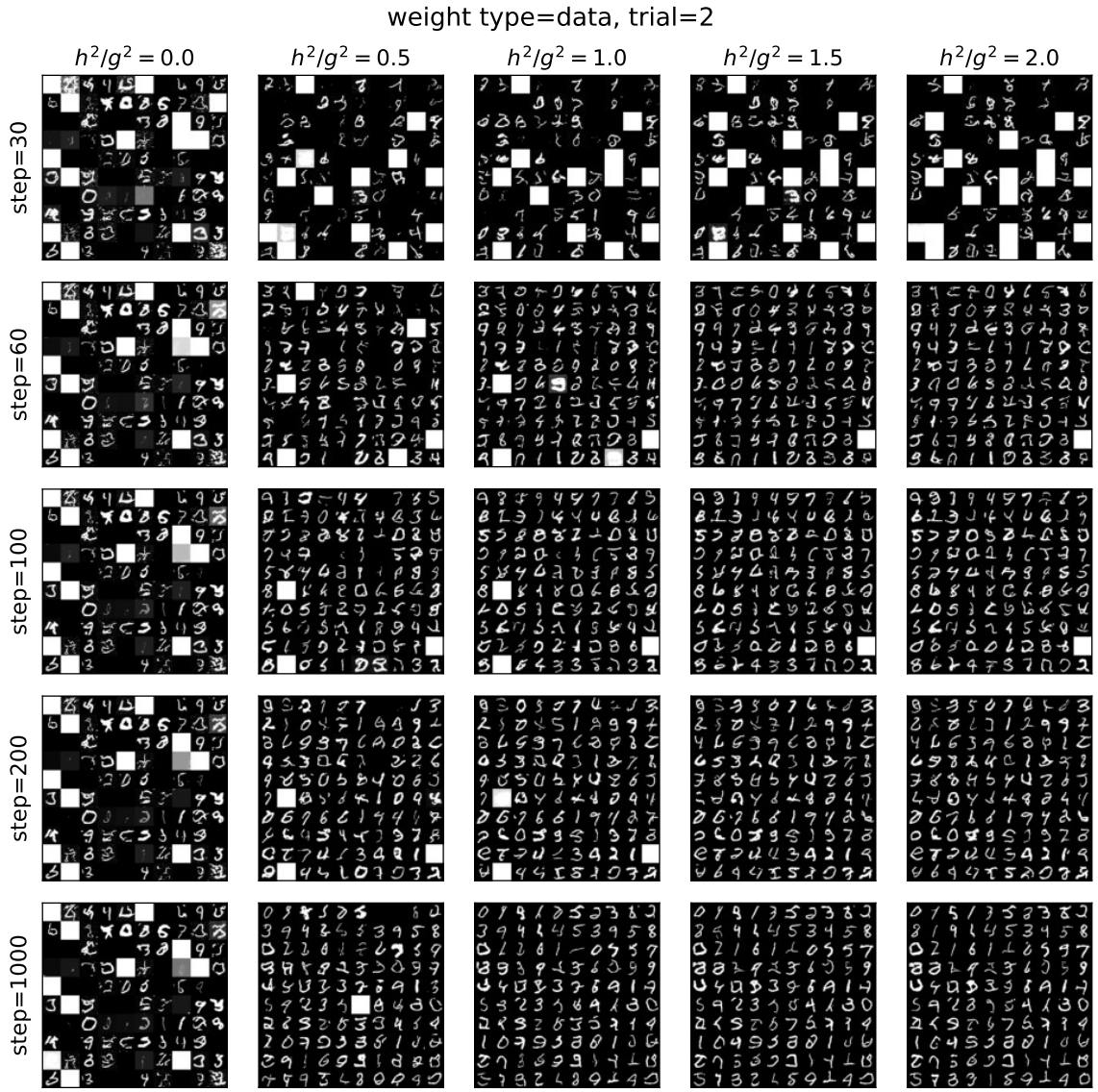


FIGURE 14. Visualization of sample generation in MNIST where we used **data-driven weight** ω (41). We use different random seed to ensure robustness and this is the result for trial 2.

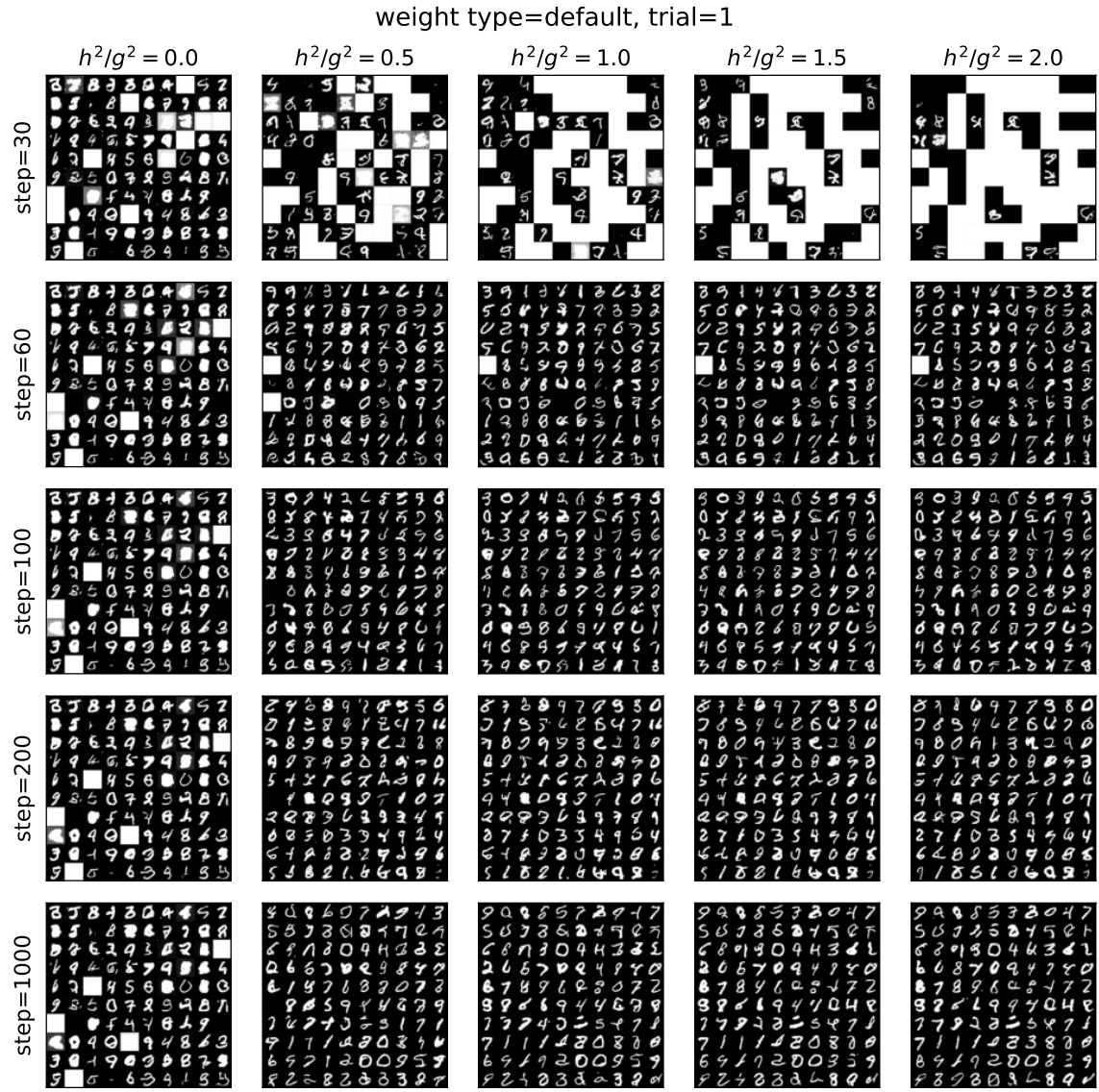


FIGURE 15. Visualization of sample generation in MNIST where we used **default weight** ω (40). We use different random seed to ensure robustness and this is the result for trial 1.

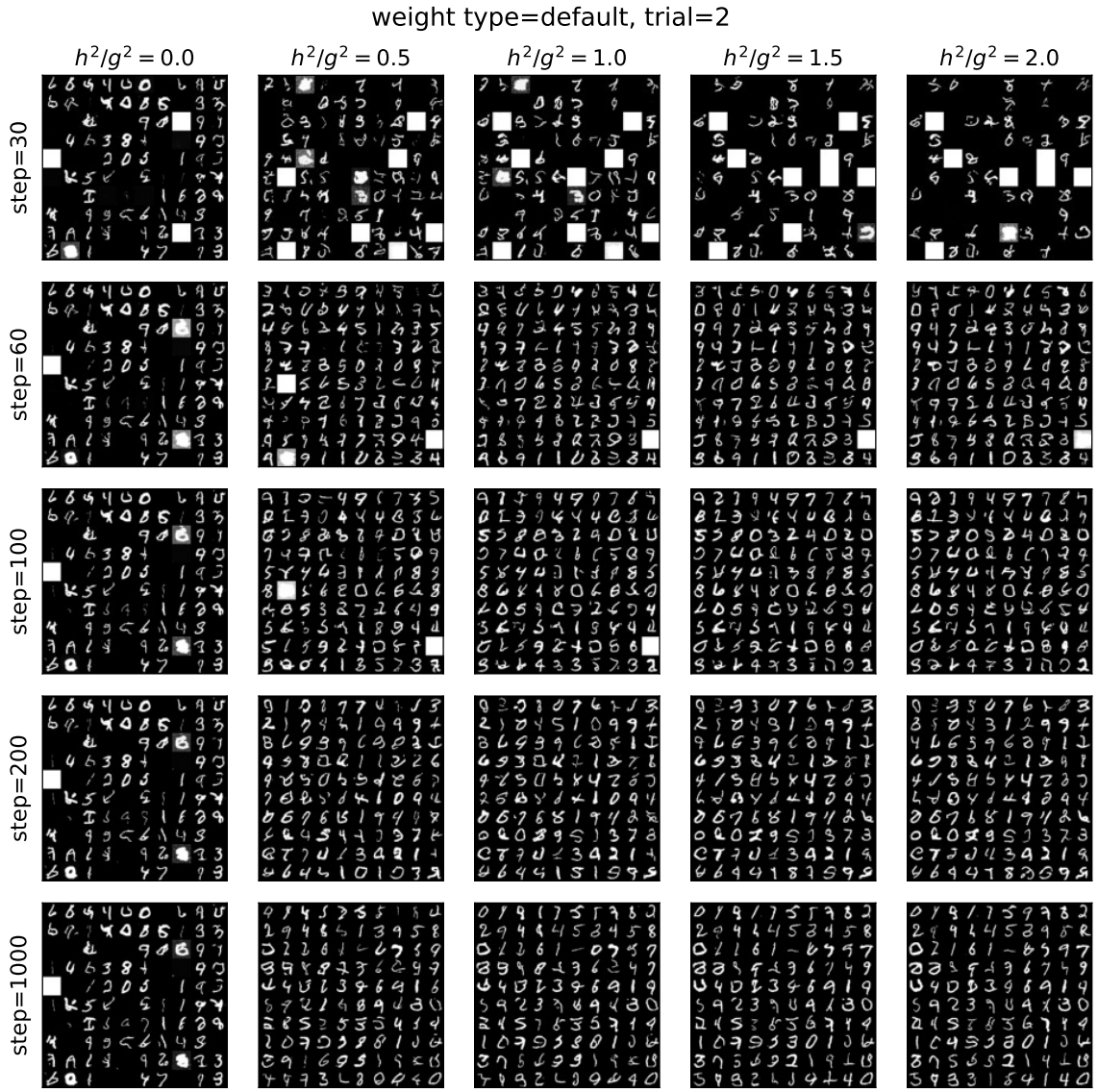


FIGURE 16. Visualization of sample generation in MNIST where we used **default weight** ω (40). We use different random seed to ensure robustness and this is the result for trial 2.

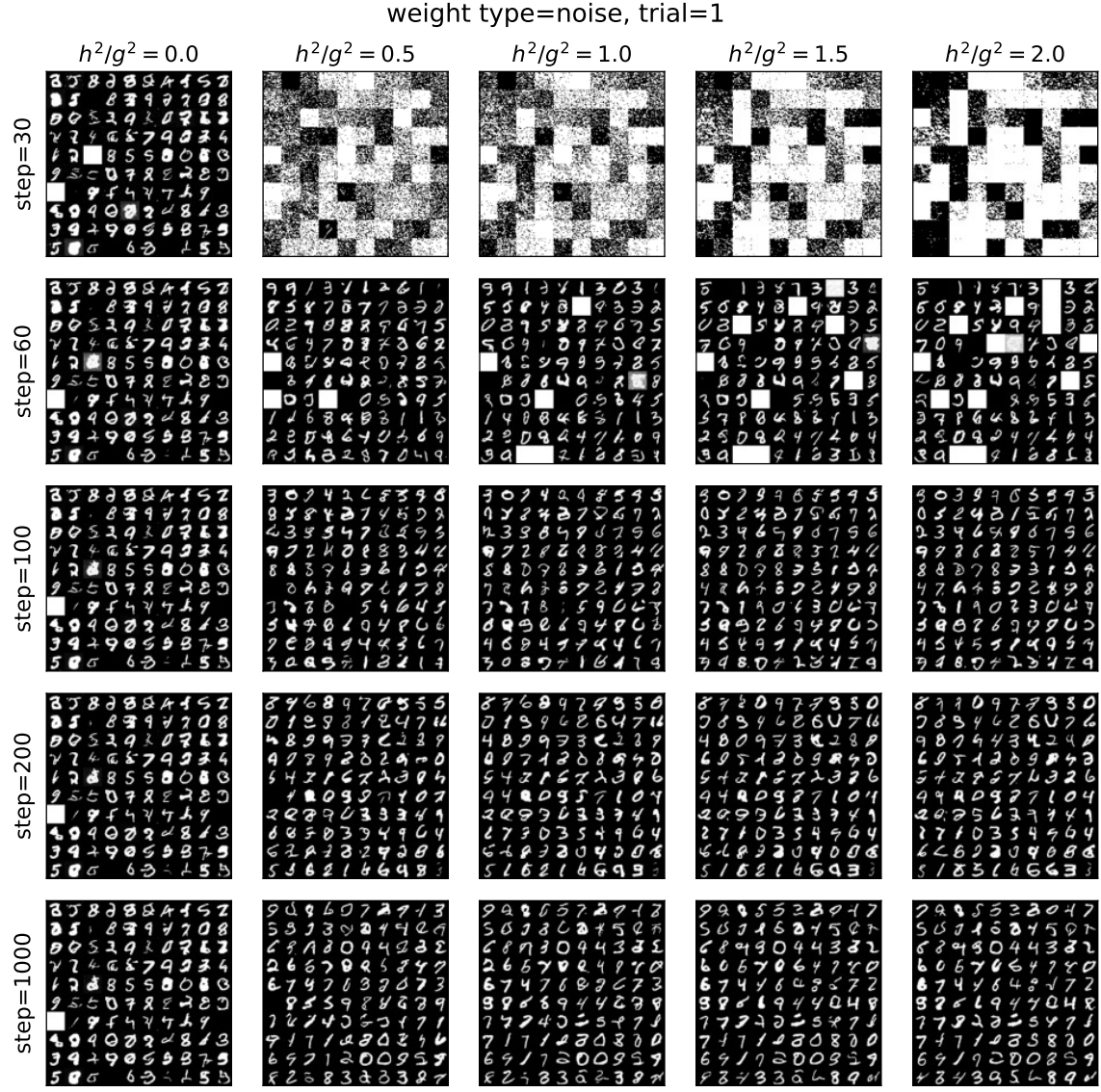


FIGURE 17. Visualization of sample generation in MNIST where we used **noise-driven weight** ω (41). We use different random seed to ensure robustness and this is the result for trial 1.

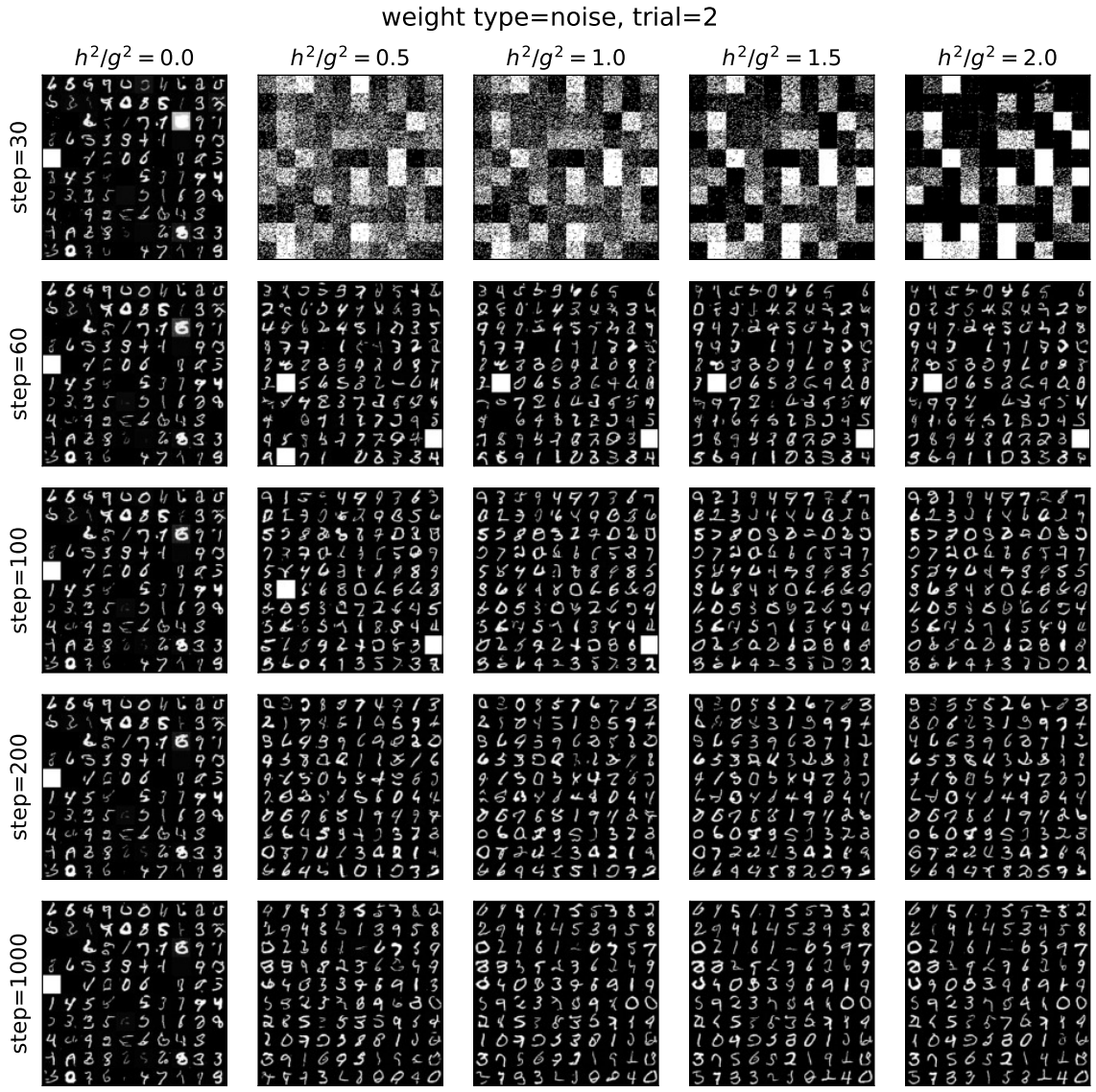


FIGURE 18. Visualization of sample generation in MNIST where we used **noise-driven weight** ω (41). We use different random seed to ensure robustness and this is the result for trial 2.